

RESEARCH ARTICLE

10.1002/2016JD025191

Key Points:

- Three-dimensional modeling of polar stratospheric clouds simulates denitrification, dehydration, and cloud coverage within error bars of observations
- CALIPSO PSC algorithm misclassifies ice PSCs into the Mixed composition categories under dehydrated and denitrified conditions
- Both the simulations and the observations suggest two major NAT formation mechanisms in the Antarctic 2010 winter

Correspondence to:

Y. Zhu,
yunqian.zhu@colorado.edu

Citation:

Zhu, Y., O. B. Toon, M. C. Pitts, A. Lambert, C. Bardeen, and D. E. Kinnison (2017), Comparing simulated PSC optical properties with CALIPSO observations during the 2010 Antarctic winter, *J. Geophys. Res. Atmos.*, 122, 1175–1202, doi:10.1002/2016JD025191.

Received 11 APR 2016

Accepted 3 JAN 2017

Accepted article online 5 JAN 2017

Published online 28 JAN 2017

Comparing simulated PSC optical properties with CALIPSO observations during the 2010 Antarctic winter

Yunqian Zhu¹ , Owen B. Toon^{1,2}, Michael C. Pitts³, Alyn Lambert⁴, Charles Bardeen⁵ , and Douglas E. Kinnison⁵ 

¹Laboratory for Atmospheric and Space Physics, University of Colorado Boulder, Boulder, Colorado, USA, ²Department of Atmospheric and Oceanic Sciences, University of Colorado Boulder, Boulder, Colorado, USA, ³Langley Research Center, Hampton, Virginia, USA, ⁴Jet Propulsion Laboratory, California Institute of Technology, Pasadena, California, USA, ⁵National Center for Atmospheric Research, Boulder, Colorado, USA

Abstract We simulate polar stratospheric clouds (PSCs) during the Antarctic winter of 2010 using the Specified Dynamics version of the Whole Atmosphere Community Climate Model/Community Aerosol and Radiation Model for Atmospheres (SD-WACCM/CARMA) model. The current PSC model contains microphysical schemes for supercooled ternary solutions (STS) and nitric acid trihydrate (NAT) particles, as well as a prognostic treatment for PSC ice particles and dehydration. Our simulations and CALIPSO satellite data suggest two major NAT particle formation mechanisms. The first mechanism is the nucleation of NAT from STS. Our model, with homogeneous nucleation rates of NAT from STS constrained by observations from the Arctic winter of 2010–2011, reproduces optical properties observed by CALIPSO over Antarctica in May and the timing of denitrification observed by the Microwave Limb Sounder within their uncertainties. On the other hand, the CALIPSO data indicate that our simulations are missing clouds containing small NAT particles with large number densities. We suggest these particles are most likely to form from ice clouds or STS in gravity waves, as found by previous investigations. The simulated cloud coverage agrees with the CALIPSO cloud coverage within a few percent on average with a correlation coefficient of 0.83. However, using the CALIPSO classification algorithm, simulated ice clouds often fall into Mix categories under the denitrified and dehydrated conditions. The model needs an improved ice microphysical representation, not only to allow ice particles to be a source of NAT but also to provide information on ice cloud particle number and size so that ice cloud optical properties can be more precisely calculated for comparison with CALIPSO data.

1. Introduction

Polar stratospheric clouds (PSCs), which can have horizontal dimensions comparable to those of the United States and extend a few kilometers vertically, have been observed in the Arctic and Antarctic for at least a century [Stanford and Davis, 1974]. However, their geographic and temporal distributions were first determined clearly by satellite observations [McCormick *et al.*, 1982]. After the Antarctic ozone hole was discovered [Farman *et al.*, 1985], PSCs drew attention because of their important roles in polar ozone depletion. Their most significant role is providing the surface area for heterogeneous chemistry [Solomon *et al.*, 1986]. Clouds composed of supercooled ternary solutions (STS; or Type Ib), as well as sulfuric acid aerosol, can efficiently promote heterogeneous reactions because their surface areas are relatively large [Hanson *et al.*, 1994; Kawa *et al.*, 1997; Kühl *et al.*, 2004; Wegner *et al.*, 2012; Solomon *et al.*, 2015]. Water ice PSCs (Type II) may provide even greater surface area for heterogeneous chemistry, but in the Arctic ice PSCs are only present sporadically, and in the Antarctic it is likely that chlorine activation has completed on the surfaces of other types of PSCs before ice PSCs form [Wegner *et al.*, 2012; Solomon *et al.*, 2015]. Although the main heterogeneous chemical processes are similar between the Arctic and the Antarctic, the wintertime Antarctic polar vortex is generally colder, more stable, and longer lasting than the Arctic vortex due to the weaker planetary wave activity in the Southern Hemisphere. The colder temperatures are associated with stronger denitrification inside the Antarctic vortex and larger ozone depletion in the Antarctic springtime [Solomon *et al.*, 2014].

Denitrification, a redistribution of HNO₃ vapor caused by the sedimentation of HNO₃-containing PSC particles, promotes ozone depletion by reducing total reactive nitrogen NO_y, which retards the deactivation of halogen-based compounds [Toon *et al.*, 1986]. Large NAT (nitric acid trihydrate; or Type Ia) particles, often called NAT-rocks due to their super-micron particle sizes [Fahey *et al.*, 2001] (radii around 10 μm or larger), play an important role in denitrification [Toon *et al.*, 1990; Waibel *et al.*, 1999; Carslaw *et al.*, 2002]; although,

their number densities can be quite small. Zhu *et al.* [2015] simulated NAT-rock particles in the 2010–2011 Arctic winter using a homogeneous surface nucleation scheme modified from Tabazadeh *et al.* [2002]. It is also possible to nucleate NAT from STS heterogeneously due to the presence of micrometeorites in the stratosphere [Hoyle *et al.*, 2013; Grob et al., 2014]. Numerical simulations by Höpfner *et al.* [2006b] and Eckermann *et al.* [2009] compared with MIPAS (the Michelson Interferometer for Passive Atmospheric Sounding) PSC observations suggest that over the Antarctic Peninsula and Ellsworth Mountains, ice PSC formation is triggered and heterogeneous nucleation of NAT particles occurs on, or in, the ice particles. As the ice evaporates in warmer regions downstream of its formation region, submicron-sized NAT particles with large number densities may be released. NAT particles nucleated on ice particles in mountain waves might also denitrify the lower stratosphere significantly if they remain at cold temperature for several days to grow larger [see also Dhaniyala *et al.*, 2002; Fueglistaler *et al.*, 2002]. Note that there are two different variations of NAT, namely, the metastable α -NAT and the thermodynamically stable β -NAT, and both may occur in the stratosphere [Tizek *et al.*, 2004]. NAT in this study probably refers the thermodynamically stable phase β -NAT.

Dehydration, a redistribution of water vapor caused by the sedimentation of ice PSC particles, inhibits ozone depletion by reducing heterogeneous (chlorine-activating) processing rates because of decreased solubility of HCl and HNO_3 in water-poor STS droplets [Wegner *et al.*, 2013] and by depressing the NAT equilibrium formation temperature [Chipperfield and Pyle, 1998]. As the temperature falls below the frost point (T_{ice}), ice containing PSC particles form. Dehydration is frequently observed in the Antarctic polar vortex [Kelly *et al.*, 1989; Vömel *et al.*, 1995] with variation in the spatial distribution and timing from year to year [Nedoluha *et al.*, 2000]. Dehydration is more evident in the Antarctic vortex than the Arctic vortex [Kelly *et al.*, 1990].

Many in situ (balloon and aircraft) and remote sensing measurements have been conducted to obtain PSC particle sizes, phases, and other properties since the last century. The Cloud-Aerosol Lidar with Orthogonal Polarization (CALIOP) on the Cloud-Aerosol Lidar and Infrared Pathfinder Satellite Observation (CALIPSO) [Winker *et al.*, 2007, 2009] satellite is one of the most important sources of such data. We refer to CALIPSO in this paper to mean the same thing as CALIOP. CALIPSO detects PSC by measuring backscatter and depolarization. The CALIPSO PSC algorithm is able to provide detailed vertical and spatial distributions of PSCs and has identified preferred locations for PSCs occurrence. Observations in 2006 by CALIPSO [Pitts *et al.*, 2007] combined with CloudSat [Wang *et al.*, 2008] show that PSCs have the highest occurrence frequency over the Antarctic Peninsula and over the ice sheets of the East Antarctic. Using backscatter and depolarization information, CALIPSO is also able to classify PSCs into different categories. Pitts and Poole [2014] use CALIPSO observations averaged over 2006 to 2014 to show that in the Antarctic STS is the main component of PSCs in the early and late winter; lower number density NAT mixed with STS dominates at the lowest altitudes throughout the winter season, while higher number density NAT mixtures with STS dominates the PSCs above ~ 20 km from late June to early September. CALIPSO finds that ice PSCs occur typically on relatively small geographic scales, although as noted by Pitts *et al.* [2013], the CALIPSO algorithm likely underestimates the occurrence of ice PSCs in denitrified and dehydrated conditions that are common during much of the Antarctic winter/early spring season.

In this paper, we use a PSC microphysical model within a global atmospheric chemistry and climate model [Zhu *et al.*, 2015] to simulate PSC formation in the 2010 Antarctic winter. We compare the simulated PSC distribution and evolution with CALIPSO observations to investigate the following questions aimed at providing further improvements for both our model and CALIPSO PSC retrieval methods:

1. How well does the CALIPSO composition algorithm work? CALIPSO does not directly measure the PSC compositions but infers them from the CALIPSO optical measurements.
2. How well do CALIPSO and the model determine the geographic area covered by PSCs and each constituent of the PSCs?
3. What are the important formation mechanisms for NAT PSCs in Antarctica and what processes need to be included for further development of the PSC model?
4. Does the NAT homogeneous nucleation scheme developed for the Arctic [Zhu *et al.*, 2015] do well in predicting Antarctic denitrification?
5. Does the model predict stratospheric dehydration well?

We approach questions 1 and 2 by applying the CALIPSO algorithm to simulations of the Antarctic PSCs for the winter of 2010 that includes dehydrated and denitrified conditions. We approach question 3 by

comparing model simulations of cloud properties with observations from CALIPSO. We approach questions 4 and 5 by comparing the simulated gas-phase nitric acid and water vapor with Microwave Limb Sounder (MLS) observations.

2. Data Description

2.1. Description of CALIPSO and Its Data Algorithms

CALIPSO data have been used extensively to study PSCs [e.g., Pitts *et al.*, 2007, 2009, 2011]. CALIOP is a two-wavelength, polarization sensitive lidar that provides high vertical resolution profiles (60–180 m for the lower stratosphere) [Winker *et al.*, 2007]. CALIPSO measures the backscatter coefficients at 532 and 1064 nm and for two orthogonal (parallel and perpendicular) polarization components at 532 nm [Winker *et al.*, 2007].

The CALIPSO PSC detection has several fundamental limitations. The temporal resolution is low at a given location, since the orbit repeats every 16 days, and only nighttime observations can be used because of lower signal to noise ratios during daylight observations. Note that polar night does allow two observations per day on ascending/descending orbits at same location at particular latitudes. Also, the orbit does not allow CALIPSO to see poleward of 82°S, and the orbit paths diverge away from the pole so that the region equatorward of 70°S is sparsely covered on any given day. These orbital constraints make it difficult for CALIPSO to determine the spatial coverage of PSCs over the entire vortex.

Another detection issue is related to the depolarization measurements of CALIPSO. It was found by Browell *et al.* [1990] that visible wavelength depolarization measurements often indicated that no solid particles were present in PSCs, when simultaneous near-infrared depolarization measurements revealed that solid particles were present. Toon *et al.* [2000] explained this observation by noting that the backscatter by NAT particles larger than 1 μm was wavelength independent between visible and near infrared wavelengths, while the backscatter of STS particles smaller than 1 μm was strongly wavelength dependent. As a consequence, STS particle backscatter can overwhelm that of NAT rocks in the visible, while NAT becomes more evident at infrared wavelengths. The practical implication of this interplay between STS and NAT is that lidars with only visible channels for depolarization can fail to observe NAT rocks embedded in STS clouds in the context of CALIPSO [Pitts *et al.*, 2009, 2011, 2013; Lambert *et al.*, 2012]. As noted by Lambert *et al.* [2012], CALIPSO also may fail to detect NAT when large NAT particles are present along with background sulfate aerosols.

In addition to limitations with the basic CALIPSO measurements, there are also challenges in using the measurements to learn about quantities that are not directly measured. Pitts *et al.* [2009, 2013] developed an algorithm to detect and classify PSC compositions by defining thresholds for scattering ratio and depolarization ratio for various categories of PSCs. These algorithms work well under the conditions of humidity and nitric acid for which they were designed. However, as we discuss below, and as mentioned by Pitts *et al.* [2013], the algorithms can have problems under perturbed conditions, which unfortunately may be common in the Antarctic wintertime.

Another important product of CALIPSO is the area of the Earth covered by PSCs, which represents the area with active heterogeneous chemistry. For the CALIPSO cloud coverage calculation, we define each 1.9° latitude ring from the South Pole toward the equator as one area section. For each day and altitude, we interpolate the CALIPSO PSC detections into each latitude ring. The frequency of the PSCs is the ratio of the number of PSCs that are observed to the number of CALIPSO observations in each latitude ring. The cloud coverage is calculated by multiplying the area by the frequency of PSCs in each latitude ring and then summing the areas for each day and altitude. This method was developed by the CALIPSO team as an improvement of their earlier methods [Pitts *et al.*, 2007, 2009]. The estimated area can be defined for all PSCs and for PSCs of a given compositional category based on the CALIPSO compositional classification algorithms.

In this paper, we use the CALIPSO lidar level 2 polar stratospheric cloud (PSC) data product, which includes perpendicular backscatter coefficient, total backscattering ratio, and particulate depolarization ratio along CALIPSO orbit tracks. The total backscattering ratio, R_{532} , is the ratio of total volume backscatter at 532 nm to the molecular backscatter coefficient at 532 nm. The particulate depolarization ratio is the ratio of the perpendicular to parallel component of the particulate backscatter coefficient. These data are used by the CALIPSO team [Pitts *et al.*, 2009] to infer PSC composition.

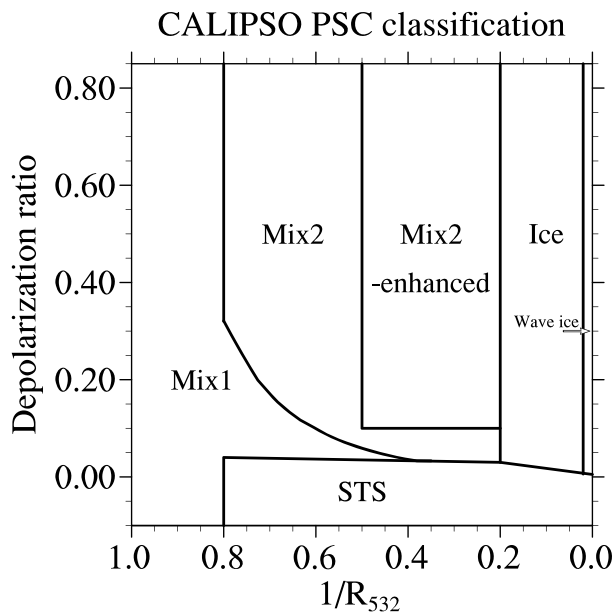


Figure 1. The CALIPSO classification for PSC compositions classifies the PSCs into four main categories (STS, Mix1, Mix2, and ice) and two subsets (Mix2-enhanced and wave ice). The mixed categories represent STS mixed with increasing amounts of NAT.

data will be averaged to a larger spatial domain, up to the 135 km limit, to obtain a measurable signal. Noise not only eliminates some data points from consideration but also spreads the values of the points that are measured as discussed below. The CALIPSO detection algorithm also requires spatial coherence so that clouds must be detected over hundreds of meters in the vertical and tens of kilometers in the horizontal and not just at one measurement point.

In formulating the CALIPSO classification product, assumptions were made about the abundances of condensable species that are present. 10 ppbv of nitric acid vapor, 5 ppmv of water vapor, and 10 cm⁻³ of total PSC number density were assumed at 50 hPa. These choices produce well-defined separations for STS, NAT, and ice in theoretical calculations of the lidar properties that are measured. However, in reality, denitrification and dehydration yield a range of values for these abundances, and the actual concentrations of particles vary with altitude even when the gas phase mixing ratios are fixed.

The CALIPSO PSC classification algorithm [Pitts et al., 2009, 2011, 2013] has six regions of the space in inverse backscatter ratio at 532 nm ($1/R_{532}$) versus depolarization plots as shown in Figure 1.

A CALIPSO measurement will be classified as STS, the only liquid PSC constituent, if it exceeds the backscattering ratio threshold, and there is no detectable enhancement in perpendicular backscatter coefficient [Pitts et al., 2013]. Clouds labeled as STS may still contain NAT [Pitts et al., 2009], with the amount of NAT not being sufficient to impact the optical properties enough to allow it to be detected.

Pitts et al. [2009] define three classes for NAT/STS mixtures in which the depolarization of the NAT is evident at visible wavelength (532 nm). Mix1 is STS (or sulfate aerosol) mixed with NAT that is not strongly backscattering. Mix2 is STS mixed with NAT that is strongly backscattering. Pitts et al. [2009] suggest that clouds with higher NAT number density or volume than a cloud with 10^{-3} particles cm⁻³ and a radius of 7 μm would fall into the Mix2 group if mixed with 10 cm^{-3} STS particles with a size that is in equilibrium with the 10 ppbv of nitric acid vapor and the ambient temperature. Mix2-enhanced is a subset of Mix2 clouds, in which NAT has sufficient number density ($>0.1 \text{ cm}^{-3}$), and therefore smaller size, to be highly backscattering. In addition, Mix1 includes all the particles when $1/R_{532} > 0.8$. The Mix2-enhanced NAT region is defined by $0.5 < 1/R_{532} < 0.2$ and depolarization ratio above 0.1.

The boundary between NAT mixtures and ice particles is assumed to be $1/R_{532} = 0.2$. Note that the ice clouds in the CALIPSO classification are usually assumed to be ice mixed with STS particles so that low depolarization

2.1.1. CALIPSO

Composition Classification

Pitts et al. [2009] describe CALIPSO's PSC composition detection and classification algorithms, and the algorithms are updated in Pitts et al. [2011, 2013]. Several lidar groups previously defined such algorithms, and it is challenging to anticipate every situation that might occur. To date, the CALIPSO algorithms have been very successful and led to many useful insights. The first step in the algorithm is to eliminate measurements that are too close to the noise limits to consider. This step includes determining a measured background backscatter and polarization from air not thought to contain PSCs, which varies slightly with time and altitude. PSCs, then, are defined as observations that exceed this background. If the CALIPSO signal is below the noise level for a high spatial resolution, the

ratios are possible [Pitts *et al.*, 2009]. The algorithm defines the subset wave ice, assumed to be clouds with small ice particles, when $1/R_{532} < 0.02$.

Three sources of misclassification have been identified. PSCs are sometimes misclassified due to noise, especially the particles near the boundary between two classes [Pitts *et al.*, 2009, 2013]. We add noise to values of backscatter and depolarization from our simulations to better emulate the CALIPSO data. Another source of misclassification is that lidars measuring visible wavelength depolarization can fail to detect NAT in clouds whose optical properties are dominated by STS as mentioned in section 2.1. Pitts *et al.* [2013] discuss the misclassification of ice particles into the Mix2 category due to denitrification from 10 ppbv to 5 ppbv. The denitrification limits the formation of STS and produces a lower backscattering ratio for STS compared with STS growing from a reservoir of 10 ppbv. Therefore, the STS/ice mixtures shift to the lower backscattering area where Mix2 is located. Here we identify another type of misclassification that occurs under dehydrated conditions when ice particles fall into STS-NAT mixed categories.

We use the CALIPSO algorithms to classify our model output into the various categories identified by Pitts *et al.* [2009, 2011, 2013]. Knowing the various properties that define the categories in the model allows us to identify situations in which the misdetection or misclassification may occur in CALIPSO algorithms.

2.2. Description of Aura MLS

The Microwave Limb Sounder (MLS) on board NASA's Earth Observing System (EOS) Aura satellite has been measuring the atmospheric composition since its launch in 2004 to the present [Schoeberl, 2007]. In this paper, we use the temperature, HNO_3 and H_2O of MLS version 3.3 level 2 data. The typical vertical resolution of observations in the lower stratosphere is 3.6–5.5 km for temperature, 2–3.7 km for H_2O and 3–5 km for HNO_3 . The time period considered is from 1 May to 31 October 2010. The MLS temperature systematic error (accuracy) is -2 K to $+1\text{ K}$, and the random error (precision) is $\pm 0.8\text{ K}$ from 100 hPa to 10 hPa. The MLS HNO_3 accuracy is $\pm 0.25\text{--}0.5\text{ ppbv}$ for 100–32 hPa and $\pm 0.5\text{--}1\text{ ppbv}$ for 22 hPa, and the precision is $\pm 0.7\text{ ppbv}$. For the vertical level 20–68 hPa, the MLS H_2O accuracy is 4–7% and the precision is 6–8% [Livesey *et al.*, 2011] (<http://mls.jpl.nasa.gov/>). The Aura MLS has similar temporal and spatial resolution limitations as mentioned before for CALIPSO satellite. MLS and CALIPSO are both A-train satellites and share the same orbit. MLS is several minutes behind CALIPSO.

3. Model Setup

The model setup in this work is the same as described in Zhu *et al.* [2015]. The Whole-Atmosphere Community Climate Model version 4.0 (WACCM 4.0) [Garcia *et al.*, 2007] with Specified Dynamics is coupled with the Community Aerosol and Radiation Model for Atmospheres (CARMA) [Toon *et al.*, 1988; Bardeen *et al.*, 2013] and nudged with reanalysis data from the Goddard Earth Observing System 5 (GEOS-5) [Reinecker *et al.*, 2008]. The model applies a horizontal resolution of 1.9° in latitude and 2.5° in longitude. The WACCM model uses the Model for OZone And Related chemical Tracers (MOZART) to treat 18 PSC heterogeneous chemical reactions on aerosols and PSCs [Kinnison *et al.*, 2007]. In addition, sulfur chemistry has been added to MOZART including reactions involving carbonyl sulfide, SO , SO_2 , S , HSO_3 , SO_3 , and H_2SO_4 [English *et al.*, 2011, and references therein]. For this PSC model, we replace the STS and NAT parameterizations in WACCM [Kinnison *et al.*, 2007; Wegner *et al.*, 2013] with microphysical processes in CARMA. STS forms from sulfuric aerosols through condensational growth and evaporation. NAT nucleates from STS through homogeneous nucleation. CARMA provides the surface area from sulfuric acid aerosols, STS, and NAT for heterogeneous chemistry in MOZART. The ice PSC formation and dehydration uses the prognostic treatment from WACCM, which only tracks the mass of condensed water and water vapor. Once formed, the PSC ice cloud stays in equilibrium with the gas phase H_2O . The model initializes with the results of a 5 year run of SD-WACCM to achieve stabilized stratospheric chemistry and sulfate aerosols. The simulations run from 1 May through the winter until 1 October 2010. We chose 2010 because it is a volcanically quiet year. The lack of volcanic forcing makes it easier to identify areas of the model needing improvement and issues with the CALIPSO PSC algorithms. As a base case, the nucleation scheme for NAT formation applies the slopeflat case as described in Zhu *et al.* [2015]. In this nucleation scheme, the free energies, which depend on HNO_3 mole fraction in STS and temperature, are modified slightly from the homogeneous surface nucleation scheme of Tabazadeh *et al.* [2002]. Based on simulations of denitrification in the

Arctic, Zhu *et al.* [2015] divided the Tabazadeh *et al.* [2002] nucleation free energy (ΔG) for NAT surface nucleation by 2 and then added a constant (31.725) to obtain the nucleation rate for the slopeflat case: $J_s = N_s \left(\frac{kT}{h} \right) \exp \left[-\frac{\Delta G_{NAT} + 63.45RT}{2RT} \right]$ where N_s is the mole fraction of HNO₃ on the surface of the particle, k is the Boltzmann constant, h is the Planck constant, R is the gas constant, and T is the temperature. The modifications are empirical and derived by fitting the denitrification observed in the Arctic for the winter of 2010–2011. A sensitivity test case called the “−1.5 K case” applies a temperature adjustment of −1.5 K for both PSC microphysics and heterogeneous chemical reactions as described by Zhu *et al.* [2015]. In another test called “slopeflat100,” we multiply the nucleation rate by 100 for the slopeflat case to evaluate the sensitivity of denitrification to the nucleation rate. These two test cases do not influence the water vapor and ice PSC amount because the adjustment only applies to CARMA microphysics and PSC heterogeneous chemistry but does not apply to CAM (Community Atmosphere Model) physics, where the formation of ice is determined.

In order to compare the simulated PSC properties with data from CALIPSO, we calculate the total backscattering ratio; the perpendicular backscatter coefficient; and the particulate depolarization ratio of STS, NAT, and ice particles. We calculate the backscattering coefficient for STS, as well as the perpendicular and parallel backscattering coefficient for ice and NAT using a T matrix approach [Mishchenko and Travis, 1998]. We use real refractive indices of 1.43 for STS, 1.50 for NAT, and 1.308 for ice with imaginary parts of the refractive index of 0.0 for all particles as used by CALIPSO PSC algorithm [Pitts *et al.*, 2009]. We assume NAT to be spheroids with an aspect ratio of 0.9, ice particles to be spheroids with an aspect ratio of 0.95, and STS to be spherical. In Appendix A, we show the depolarization of NAT and ice for different aspect ratio assumptions and discuss the reasons why we use these aspect ratios.

A complication in comparing the CALIPSO data with the simulations is that some of the clouds observed by CALIPSO might be smaller than a model grid cell. Our simulations assume that each constituent of cloud (STS, NAT, or ice) is spread uniformly over the grid cell and is mixed with each other. In reality, there may be ice clouds in part of a grid cell and STS or NAT clouds in another part. CALIPSO high-resolution data would distinguish the individual clouds. Alternatively, for insight, we also assume that the clouds are not mixed within a grid cell and combine these particles into their most likely groupings which are NAT/STS mixtures and ice/STS mixtures. We choose these two mixture groups because STS or sulfate aerosol have large number densities and serve as the nuclei for NAT or ice in our model.

For STS and NAT, the model provides the size distribution information needed for the optical calculations. Ice particles often have the sizes around a few microns [Dye *et al.*, 1992; Zasetsky *et al.*, 2007] and may have number densities from less than 0.1 cm^{−3} up to 10 cm^{−3}. However, our model only tracks the ice mass. In order to compute the backscatter due to ice clouds we assume that the number of ice particles is equal to 1% or 10% of the number of STS particles in the grid cell. This is equivalent to assuming that 1% or 10% of STS particles nucleate to form an ice particle when an ice cloud forms. For example, if 2 ppmm (ppm mass, equal to 3.2 ppm volume) of water condenses to form ice at 50 hPa, and 10 cm^{−3} STS particles are present, then the size of a monodisperse ice particles will be 6.8 μm if the number density of ice is equivalent to 1% of STS. Observations of ice particles in wave clouds suggest they are smaller than 3 μm [Höpfner *et al.*, 2006a], indicating a larger fraction of the STS particles nucleate to form ice in wave clouds. However, our model cannot resolve wave clouds, so we neglect this possibility in our calculations.

An additional complication in using the CALIPSO algorithm to compare PSC composition with our simulations is that the CALIPSO algorithm is affected by measurement noise, which is not inherent to the model. Here we compute the noise for the modeled optical properties following Engel *et al.* [2013]. The backscatter coefficients (both perpendicular and parallel) with noise are estimated by picking a random number from a normal distribution with a defined expectation and standard deviation. The expectation is the same as the simulated backscatter coefficient without noise. The standard deviation (uncertainty) is estimated using the following equation:

$$\sigma(\beta) = \frac{1}{75} \beta \sqrt{\frac{2.39 \times 10^{-8} \text{ m}^{-1} \text{ sr}^{-1}}{\beta} \times \frac{1500 \text{ km}}{\Delta_{\text{horizontal}}} \times \frac{5 \text{ km}}{\Delta_{\text{vertical}}}}$$

where β is either total perpendicular or parallel backscatter coefficient and $\Delta_{\text{horizontal}}$ is the horizontal averaging distance, which we assume is 135 km. Δ_{vertical} is the vertical averaging distance, which is 180 m

for CALIPSO. The noise is calculated for each of the four components (STS, NAT, ice, and molecular) of the total backscatter coefficient.

4. Results

4.1. A Comparison of PSC Compositions Determined From Simulations and From CALIPSO Data

We use the CALIPSO detection and classification algorithm described in section 2.1.1 to analyze the PSCs simulated by the model for the Antarctic winter of 2010. We pick fixed numbers for the simulated PSC detection threshold: a backscattering ratio of 1.32 and a perpendicular backscatter coefficient of $3.28 \times 10^{-6} \text{ km}^{-1} \text{ sr}^{-1}$. The ability of the model to correctly simulate data from this winter is discussed below.

Figure 2 shows the depolarization ratio and $1/R_{532}$ from a simulation at 52 hPa (~19 km outside the vortex to 18 km inside the vortex) and from CALIPSO data at 18.7 km in July 2010. The plot of optical properties assumes that the number density of ice is 1% of STS; the WACCM model does not compute the ice number density. Figure 2a shows the CALIPSO observations with STS (red), Mix1 (purple), Mix2 (green), Mix2-enhanced (dark green), and ice clouds (blue). Figures 2b and 2c display the modeled optical properties for STS (red), NAT (purple), and ice clouds (blue) individually without and with noise. Clearly adding noise spreads the points across the histogram, creating points at higher and lower depolarization, as well as creating a wide range of backscatter values.

We interpolate the simulated PSCs onto the A-train orbit in order to have a corresponding comparison with CALIPSO data during the same period. The time period of the interpolation is synchronized with MLS, which is only about 6 min behind CALIPSO. This choice of being aligned with MLS is because the resolution of the model grid box is close to MLS resolution. On the other hand, CALIPSO has a resolution about 30 times higher than the model along the track and therefore has more cloud details. For example, CALIPSO may observe different cloud compositions occupying different fractions in 30 observed points, while the model only has one point of data. Figure 2c might be most relevant for comparison to CALIPSO data if clouds of differing composition were in fact separated in space within each model grid cell. Figure 2c clearly illustrates where different constituents of clouds occur on this diagram. Most notable is that the points CALIPSO attributes to Mix2 and Mix2 enhanced (NAT/STS mixtures) are ice clouds in our model. Another difference is that the model does not produce many ice clouds with $1/R_{532}$ smaller than 0.15 as seen in CALIPSO.

To understand the reasons that ice particle clouds or ice/STS mixtures are classified in Mix2 or Mix2-enhanced categories (NAT/STS mixtures), we explore the optical characteristics of STS and ice/STS mixtures. From the middle to the end of the winter season in the Antarctic, the polar stratosphere is often dehydrated from ~5 ppmv to ~2 ppmv by ice clouds in the coldest regions. Dehydration inhibits the formation of STS particles. Figure 3 (top) shows the STS radii changing with temperature under different water vapor and HNO_3 assumptions. STS is calculated using 10 or 5 ppbv of HNO_3 and 5 or 2.75 ppmv of H_2O at 50 hPa by an equilibrium model [Carslaw *et al.*, 1995] assuming no NAT is formed. With 10 ppbv of HNO_3 and 5 ppmv of water vapor, STS starts to grow significantly below 191.5 K. In denitrified condition, the STS starts to grow below 191 K and the size is about 0.1 μm smaller from 185 K to 191 K than if 10 ppbv of nitric acid were present. Under dehydrated condition, the STS particles do not add significant mass above 189 K. If the atmosphere is denitrified and dehydrated at the same time, STS particles have even smaller sizes under the same temperature and pressure conditions.

Figure 3 (bottom) shows how the depolarization ratio versus $1/R_{532}$ of ice/STS mixtures varies for different assumptions of the mixtures of ice and STS. The four different colors in Figure 3 (bottom) represent STS under unperturbed, dehydrated, denitrified, and dehydrated and denitrified conditions as shown in Figure 3 (top). For each case, we assume ice particles with various radii and number densities to calculate the backscatter and depolarization coefficient (the radii and number densities are marked in Figure 3). The calculation of STS backscattering coefficient uses the radii in Figure 3 (top) at 185 K and assumes a total PSC number density of 10 cm^{-3} . In other words, for each STS/ice mixed cases, the total H_2O is 5 or 2.75 ppmv of gas phase H_2O plus the condensed water that is in ice particles; the number density of STS is 10 cm^{-3} minus the number density of ice particles. Under the unperturbed case (orange), all the points are within the area with $1/R_{532} < 0.2$. The dehydrated (blue) and denitrified (green) conditions show a relatively higher depolarization and lower backscattering ratio (higher $1/R_{532}$) due to smaller STS compared to the unperturbed condition.

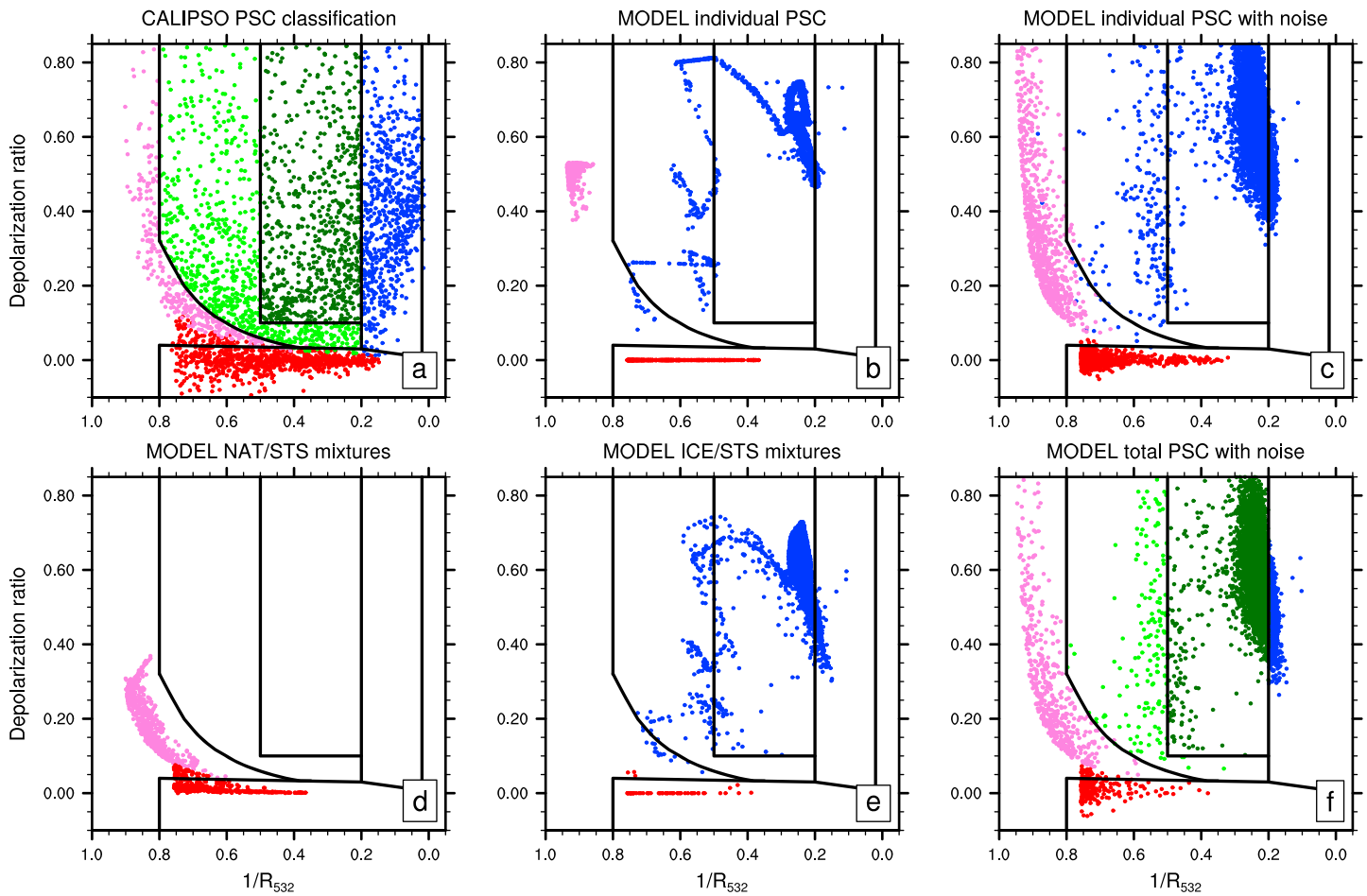


Figure 2. The depolarization ratio versus $1/R_{532}$ at 18.7 km (52 hPa) in July 2010. (a) The CALIPSO defined STS is in red, Mix1 in purple, Mix2 in green, Mix2 enhanced in dark green, and ice in blue [Pitts et al., 2009]. (b) The modeled PSC constituents individually with STS in red, NAT in purple, and ice in blue. (c) Figure 2b with noise. (d and e) The modeled NAT/STS mixtures and ice/STS mixtures. The red points are clouds with $R_{532} > 1.32$ and perpendicular backscatter coefficient $< 3.28 \times 10^{-6} \text{ km}^{-1} \text{ sr}^{-1}$. The blue and purple points in Figure 2c are clouds with perpendicular backscatter coefficient $> 3.28 \times 10^{-6} \text{ km}^{-1} \text{ sr}^{-1}$. (f) The optical properties assuming all the constituents are mixed in a grid cell and include noise. The colors represent the same thresholds as defined in Figure 2a.

When the air is dehydrated and denitrified at the same time, the simulated ice/STS mixtures show a significant shift to the lower backscattering ratio (higher $1/R_{532}$). Therefore, due to the denitrification and dehydration in Antarctic winter midseason, Mix2 and Mix2-enhanced categories may contain lots of ice and ice-containing mixtures.

Figure 2f shows the same simulation from which the optical properties of the individual constituents are computed in Figure 2c, but assumes all of the clouds are present over the entire grid cell, and includes experimental noise. In this case one cannot simply identify a composition attached to one point, since several different cloud constituents are present in each grid cell. The colors in Figure 2f represent the CALIPSO classification categories as in Figure 2a. Note that the red dots covering STS and a small part of Mix1 occur because the boundary between STS and Mix1 depends on the perpendicular backscatter. Nevertheless, the general distribution of particles in Figures 2c and 2f are similar, except less STS is shown in Figure 2f. There is less STS in Figure 2f because some STS particles are mixed with NAT or ice increasing the depolarization ratios for those mixtures. Figures 2c and 2f indicate that the modeled ice dominates much of the regions attributed to ice, Mix2 or Mix2 enhanced by the CALIPSO algorithm. This ice distribution feature is also shown in Figures 2b and 2e, where STS provides some backscatter contribution, but ice provides the most backscatter and depolarization. This result can be modified if we assume a different fraction of STS particles nucleate to form ice than the 1% taken in Figures 2b and 2e. Figure 4a illustrates an assumption that the ice number density equals to 10% of the STS number density. In this case more ice points lie in the ice domain of Figure 4

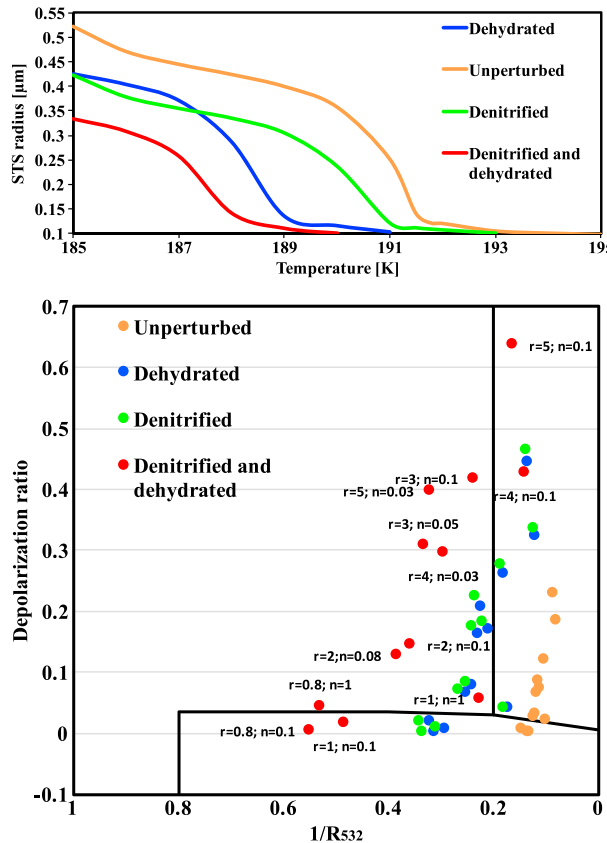


Figure 3. (top) The STS radius variation as a function of temperature under unperturbed (H_2O 5 ppmv and HNO_3 10 ppbv), dehydrated (H_2O 2.75 ppmv and HNO_3 10 ppbv), denitrified (H_2O 5 ppmv and HNO_3 5 ppbv), and denitrified and dehydrated (H_2O 2.75 ppmv and HNO_3 5 ppbv) conditions calculated from the equilibrium model [Carslaw et al., 1995]. (bottom) The depolarization ratio versus $1/R_{532}$ for STS/ice mixtures at 185 K. The backscatter of STS is calculated using the radius in Figure 3 (top) at 185 K with corresponding colors. The backscatter and depolarization of ice are calculated with various radii (r) in μm and various number densities (n) in cm^{-3} . The points represent combinations of STS and ice backscatter. We only mark the r and n for the denitrified and dehydrated (red dots) condition. The r and n correspond to a single size and radius rather than a size distribution.

Mix2-enhanced area. Producing more NAT particles results in fewer particles that are identified as STS. One of the reasons for the reduction in STS is that more NAT particles exist within the STS clouds increasing the depolarization for that area. Also, when more NAT particles exist, they pull the HNO_3 from the STS particles because the vapor pressure is lower over NAT particles, causing the STS to evaporate. It is possible that additional NAT nucleation mechanisms, such as by evaporation from ice clouds, might produce higher number density NAT clouds with smaller particle sizes. In order to make a better comparison with the CALIPSO observations, the model needs to include a microphysical model for ice that includes release of NAT from ice as discussed below.

Another question is whether some PSCs seen by the model are not included in the PSC category by the CALIPSO detection threshold. Figure 5 shows the modeled sulfate aerosol/STS/NAT mixtures' inverse backscattering ratio and depolarization ratio from the base case (detailed in section 3). The color of the points represents the NAT (e.g., $\text{HNO}_3\text{-3H}_2\text{O}$) mass mixing ratio in those particles. The dashed lines are typical boundaries for PSC cloud detection in the CALIPSO algorithm, which means that all the simulated particles located on the left side of the dashed line fall below the detection threshold in the CALIPSO classification scheme. The detection threshold is dependent on both backscattering ratio and perpendicular backscatter. The perpendicular backscatter is not an axis in this diagram, so the dashed lines may vary slightly with

a than in Figure 2e, and many points are within the region with $1/R_{532}$ smaller than 0.15 where ice is seen in CALIPSO observations. Therefore, some of the ice particles in the model should have larger number density and smaller sizes to create larger backscattering ratio. Unfortunately, there are no constraints on the number of ice particles that nucleate, and it is likely to be highly variable because it may depend on the cooling rate as it does for cirrus cloud formation [Jensen and Toon, 1994]. It is important to add microphysical processes for ice in the model to track the number densities and radii.

Figure 2d illustrates the optical properties of NAT/STS mixtures assuming ice is not present. As can be seen, the STS reduces the mixed cloud depolarization but moves the value of $1/R_{532}$ to the right (lower values), but there is larger backscatter compared with Figure 2b. In Figures 2c, 2e and 2f, NAT clouds are mainly located in the Mix1 cloud area, because the homogeneous nucleation scheme in our model generates NAT with number densities around $10^{-3} \sim 10^{-4} \text{ cm}^{-3}$ [Zhu et al., 2015]. Figure 4b illustrates a test assuming the nucleation rate of NAT is 100 times larger than assumed in Figure 2. In this case more NAT particles are found in the Mix2 area, but we still have no NAT appearing in

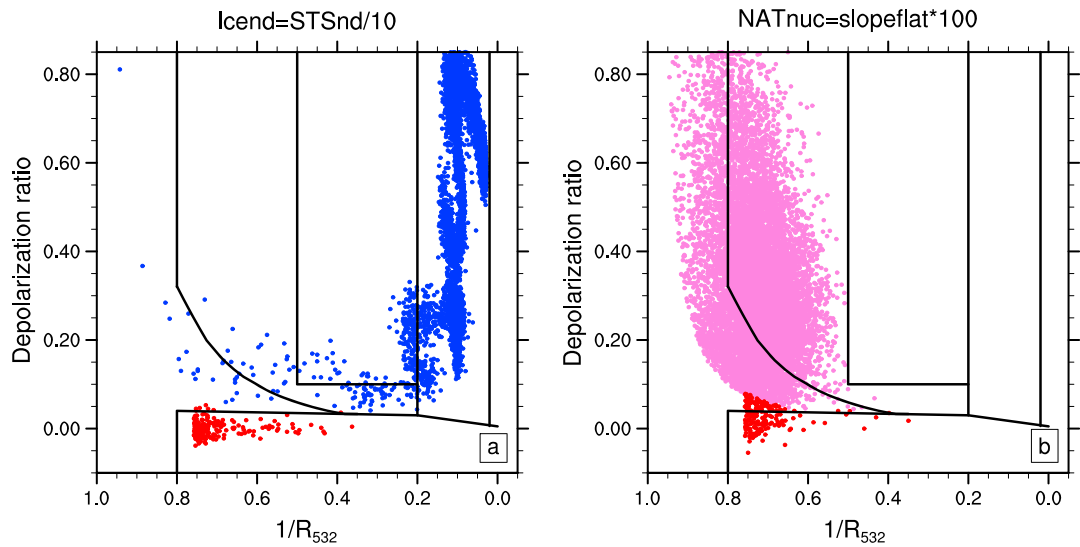


Figure 4. The depolarization ratio versus $1/R_{532}$ from two model cases. (a) The simulated ice/STS mixtures when ice number is 10% of STS number density. (b) The simulated NAT/STS mixtures with NAT nucleation rate of slopeflat100.

temperature or pressure due to the variation of molecular backscatter coefficient. Figure 5 indicates that considerable masses of large NAT particles (lower than 5 ppbm) are possible to be in the regions which CALIPSO excludes because of signal to noise issues as addressed by Pitts *et al.* [2013]. The model often predicts low number density of NAT, and the backscattering ratios of those particles are not high enough to exceed the noise level. Those NAT particles are responsible for denitrification because of their large sizes. Another point from this figure is that some clouds in the STS classification range have high NAT mass mixing

ratios (3–4 ppbm) due to the computed noise for depolarization. We find for the clouds containing NAT with mixing ratio over 4 ppbm in this figure that about 54% are categorized as Mix1 particles, 15% as STS, and 31% do not pass the PSC detection threshold. All the NAT particles with mixing ratio over 4 ppbm in our model have radius over $4\text{ }\mu\text{m}$ whose fall velocity is $\sim 1\text{--}2\text{ cm/s}$ and sediment $\sim 1\text{ km/d}$.

4.2. PSC Coverage for Different Cloud Categories

In this section we compare simulations with CALIPSO data throughout the winter and further discuss how well the CALIPSO classification algorithm and cloud coverage calculation may function. The duration and the vertical extent of Antarctic PSCs is similar from year to year but with some variability [Pitts and Poole, 2014]. Using the same detection and classification method described in section 4.1, we retrieve the cloud

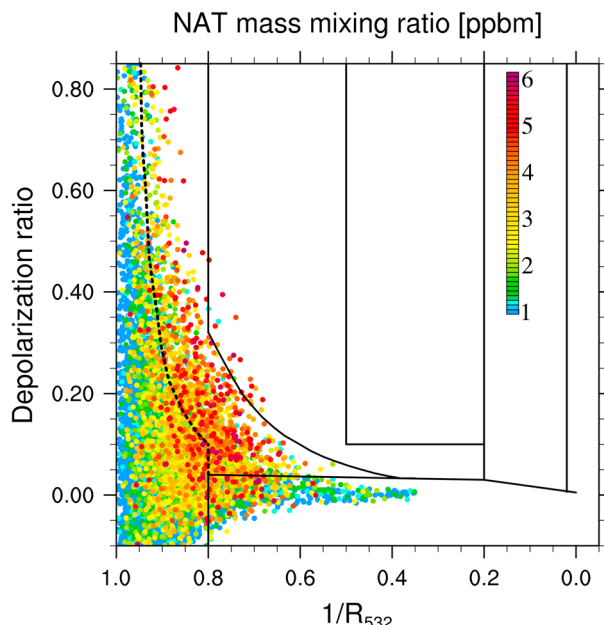


Figure 5. The depolarization ratio versus $1/R_{532}$ of the modeled sulfate aerosols/STS/NAT mixtures at 52 hPa in July 2010. The color of the dots represents the NAT mass mixing ratio in these clouds, where the molecular weight is taken from $\text{HNO}_3\text{-H}_2\text{O}$. The solid lines represent different PSC categories as defined in Figure 1. The dashed lines are the typical PSC detection thresholds.

coverage for all PSCs and for each constituent of PSCs from simulations for the 2010 Antarctic winter. We calculate the simulated daily cloud coverage at different pressure levels by assuming that PSC fills the entire model grid cell. The CALIPSO cloud coverage calculation uses the method described in section 2.1.

Figure 6 shows the area covered by clouds from 1 May to 28 October 2010, within a 15 km to 30 km altitude range and for regions equatorward of 82°S. We show the total PSC area, as well as the fraction of PSC area in the five categories defined by the CALIPSO retrieval: STS, Mix1, Mix2, Mix2 enhanced, and ice. Figures 6a1–6a6 are the CALIPSO data, Figures 6b1–6b6 are the simulated PSC coverage assuming the ice number density equals 1% of STS number density, and Figures 6c1–6c3 and 6c6 show the same model case and assumptions but assuming each individual PSC constituent (STS, NAT, or ice) is located separately in a grid box. Therefore, Figures 6c1–6c3 and 6c6 do not follow the CALIPSO categories but simply classify the modeled PSCs into STS, NAT, and ice.

As shown in Figures 6a1, 6b1, and 6c1, the PSCs appear in late May and last until late September or early October for the 2010 Antarctic winter. The CALIPSO cloud coverage shows the largest cloud coverage from mid-June to mid-July and so does the model. A second peak of high cloud coverage above 20 km altitude lasts from mid-August to the end of August in both simulations and observations. Figure 7 shows a regression plot comparing the CALIPSO observed and simulated total PSC area for each day and altitude level. We force the regression line through the 0–0 point because with simulations nudged to observed temperatures the model should not produce clouds where they do not occur. The simulated cloud coverage is within 3% of the area observed by CALIPSO, and the two coverages have a correlation coefficient of 0.831. Forcing the regression line through the 0–0 point may bias the regression for low values of area, but the model grid has a much poorer resolution than CALIPSO observations which may also lead to a bias in low area values. The colors in Figure 7 represent the altitudes of the points. The model area is larger for lower altitudes, and the CALIPSO area is larger for higher altitudes. This pattern may be associated with the missing small NAT particles in the model. Particles with smaller sizes have slower fall velocity and, therefore, would remain at higher altitude. As shown in Figures 6a3–6a5, CALIPSO indicates that the Mix2 (smaller particles) dominate at high altitudes and Mix1 (larger particles) dominate at lower altitudes. Since our simulations are missing the small NAT particles we underestimate the area at high altitude.

STS (Figure 6b2) in the model shows higher fraction in May and June in both the CALIPSO data and the simulation; however, the fraction of STS is larger in the observational data (Figure 6a2) than in the simulations (Figure 6b2). This greater observed amount may be because we cannot separate the cloud constituents within the model grid box and because clouds with high backscatter (i.e., ice clouds) mask STS if they occupy the same grid cell. If we assume each constituent of PSC is located separately in a grid cell (Figure 6c2), more STS clouds are found through the winter and the area fraction of STS is closer to the CALIPSO STS fraction. CALIPSO also finds that STS dominates in late September in the area below 18 km (Figure 6a2), but most of the clouds in this period in the simulations are in Mix and ice categories (Figures 6b3–6b6). CALIPSO observations show that Mix1 clouds (Figure 6a3) mainly dominate the lower altitudes and Mix2 clouds (Figure 6a4) dominate the higher altitudes through the winter. The simulated Mix1 (Figure 6b3) and Mix2 clouds (Figure 6b4) show a similar pattern. The NAT fraction (Figure 6c3) is very similar to Mix1 fraction (Figure 6b3), indicating that Mix1 category contains STS/NAT mixtures. The ice fraction (Figure 6c6) is about the sum of Mix2-enhanced (Figure 6b5) and ice (Figure 6b6) categories, indicating that these two categories are ice or ice/STS mixtures. The modeled Mix2 category (Figure 6b4) has a very small cloud fraction, and it probably contains STS, NAT, and ice or their mixtures. As discussed in section 4.1, the modeled cloud compositions and their categories indicate that Mix2 and Mix2-enhanced categories contain ice clouds because of denitrification and dehydration during the Antarctic winter. However, it is possible that the observed clouds in the Mix2 and Mix2-enhanced categories contain many NAT particles created from ice, a process that is missing in the model.

Different PSC constituents form at different temperatures. Therefore, we analyze PSC occurrence relevant to theoretical equilibrium temperatures [Lambert *et al.*, 2012; Pitts *et al.*, 2013] for different PSC constituents in order to have a better understanding of the CALIPSO PSC classification algorithm. Figure 8 shows the histogram of PSC occurrence from CALIPSO and the model at 490 K (~50 hPa or ~20 km) for the whole 2010 Antarctic winter. The x axis represents the difference between the ambient temperature and the theoretical equilibrium temperature. In Figures 8a and 8c, T_{ice} is the ice frost temperature [Murphy and Koop, 2005]. In Figures 8b and 8d, T_{eq} represents the ice frost temperature. NAT equilibrium temperatures are used for

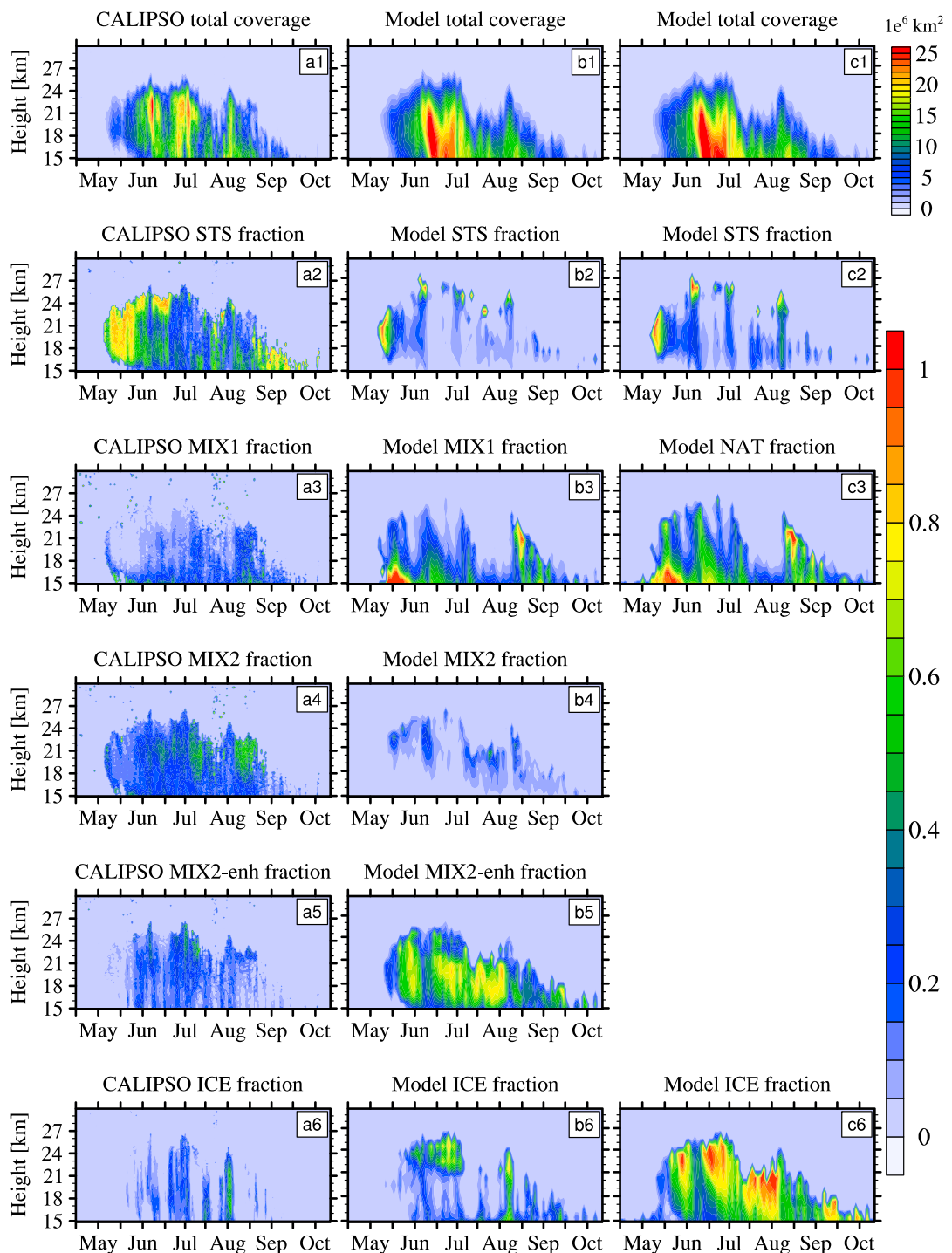


Figure 6. The PSC cloud coverage and the fraction of each classification category of PSC at different altitudes over the winter of 2010. (a1–a6) The CALIPSO data. (b1–b6) The modeled PSC using the CALIPSO classification algorithm. (c1–c3 and c6) The modeled PSC assuming each constituent of PSCs is independent. The names of the months are centered on the middle of the month.

Mix1, Mix2, and Mix2-enhanced categories [Hanson and Mauersberger, 1988], and STS equilibrium temperature is used for the STS category [Carslaw et al., 1995]. We obtain the equilibrium temperature for CALIPSO PSCs following Pitts et al. [2013]. In order to have a closer comparison with Pitts et al. [2013], we eliminate the simulated points where HNO_3 gas is less than 1 ppbv to avoid the region where STS and NAT equilibrium

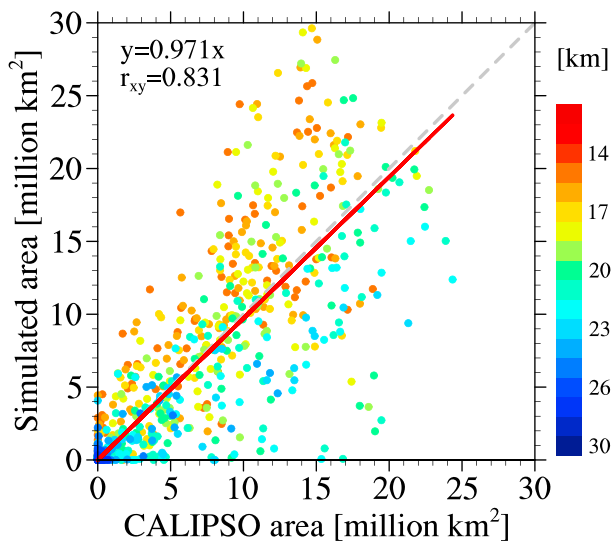


Figure 7. The 1–1 plot of total PSC cloud coverage from the simulations and from CALIPSO observations. The colors of the dots represent different altitudes. The red line is the regression line, whose equation and correlation coefficient are shown on the left corner of the plot. The grey dash line is the 1–1 line.

the simulations do not include any barrier to ice nucleation, which may exist in reality and offset the ice formation temperature from the equilibrium temperature. The peak of the histogram in CALIPSO data is about 0.5 K lower than the ice frost point, which may be because the ice particles form below the equilibrium temperature due to the energy barrier involved in nucleation and it takes time for the clouds to go back to equilibrium.

The CALIPSO data in Figures 8a and 8b show a bimodal distribution for Mix2 (orange) and Mix2 enhanced (red). The lower-temperature peak is close to ice frost point (Figure 8a), and the higher-temperature peak is close to the NAT equilibrium temperature (Figure 8b). In the simulations shown in Figure 8, the orange and red histograms almost overlap with the ice histogram at the ice frost point in Figure 8c, with little tails at temperatures slightly above the frost point. And they also show the peak around –5 K in Figure 8d. From the discussion for Figure 6, we know that the majority of particles in Mix2 and Mix2-enhanced categories are ice in the simulations and the little tails for Mix2 category contain some NAT particles existing at higher temperature. Therefore, it is likely that most of the low-temperature peak in the simulations of Mix2 and Mix2 enhanced are ice clouds. However, referring to the observations, it is possible that those clouds at the low-temperature peak contain new NAT clouds nucleated from STS or evaporated from ice and not exposed long enough to reach equilibrium [Pitts et al., 2013]. The simulations miss the higher-temperature peak because the simulations lack small NAT particles with large backscatter that would be classified in Mix2 and Mix2-enhanced categories. Those NAT particles are likely to have large enough number densities and surface areas to reach equilibrium quickly. They are likely generated from STS in the wave event or from wave-ice PSCs.

Both the simulations and the CALIPSO data in Figure 8 show that the Mix1 category covers a large temperature range, probably because the NAT particles in the Mix1 category have small concentrations and small surface areas, so they are often not in equilibrium.

The STS histogram (light blue) in Figure 8 shows the peak slightly higher than the ice frost point but ~1 K lower than the STS equilibrium temperature in both CALIPSO data and the model results. We find that because of dehydration and denitrification, the majority of STS clouds in Figure 8c have a surface area lower than $6 \mu\text{m}^2/\text{cm}^3$. The small surface areas and low nitric acid partial pressures retard growth rates and slow the time for clouds to reach equilibrium. Another minor contribution to the small size of STS in the simulations is that the model considers the curvature (Kelvin) effect when we calculate the growth rate of STS, which slows the growth of the particles.

temperature curves converge [Pitts et al., 2013]. We interpolate the locations of the simulated PSCs onto the A-train orbit and add noise to the simulated optical properties. The total PSC numbers are normalized to 1 for all the panels.

The ice number histogram in Figure 8 (dark blue) shows a peak around the ice frost temperature from both simulations and CALIPSO data. The simulations have a narrower distribution than observed in part because of the uncertainty of GEOS-5 temperature used for CALIPSO calculation. The modeled ice particles stay in equilibrium with the temperature field, and therefore $T - T_{\text{ice}}$ equals zero; however, CALIPSO needs to interpolate the GEOS-5 temperature to the CALIPSO orbit, which produces spatial and temporal uncertainty. Also,

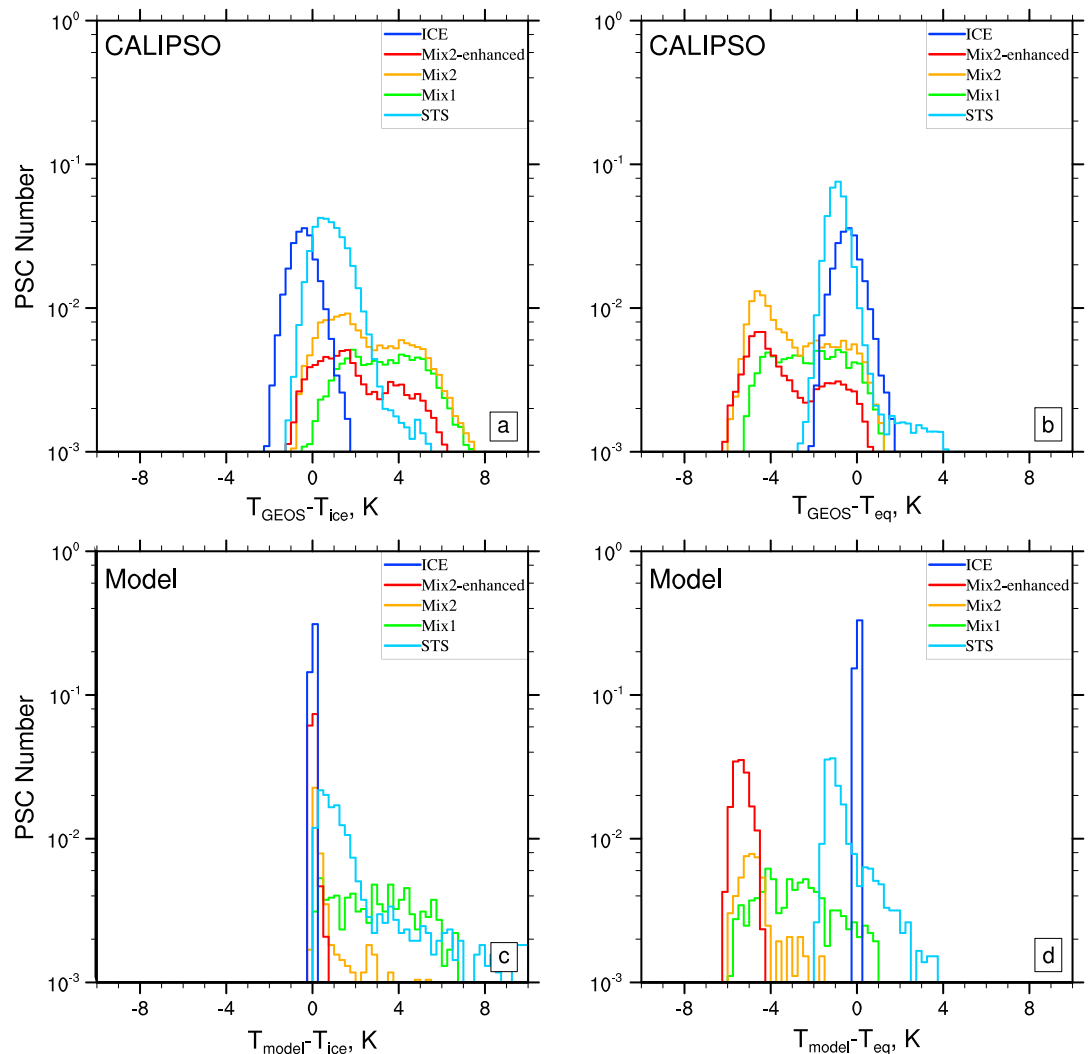


Figure 8. Histograms of CALIPSO and the simulated numbers of PSC observations at 490 K potential temperature during 2010 Antarctic winter as a function of $T-T_{\text{ice}}$ and $T-T_{\text{eq}}$. The total PSC number is normalized to 1 for each panel. The colors represent the CALIPSO PSC classification categories. (a, c) T_{ice} is the ice frost temperature. (b, d) T_{eq} represents the ice frost temperature.

4.3. The Influence of the Choice of Mechanism for NAT Formation on Denitrification Timing

The nucleation rate used in the model is based on laboratory data for free energies but was empirically tuned to explain Arctic denitrification for the winter 2010–2011 [Zhu *et al.*, 2015]. The empirically derived nucleation rate typically results in large NAT particles with small number density. In this section, we want to investigate two questions: (1) Does the model simulate large NAT particles in the Antarctic winter? (2) Does the model simulate small NAT particles in the Antarctic winter?

Our model does not include microphysical processes to produce NAT from ice PSCs nor does it have enough spatial resolution to represent temperature fluctuations from mountain waves. In the past, both processes have been suggested to form small NAT particles. Carlsaw *et al.* [1998] present data suggesting that small NAT particles are released from evaporating ice clouds formed in a wave clouds in the Arctic. Höpfner *et al.* [2006b] and Lambert *et al.* [2012] present data suggesting that ice clouds formed near the Antarctic Peninsula release small NAT particles creating a belt of small NAT particles around the edge of the continent. NAT rocks might grow from these small NAT particles and denitrify the stratosphere if the temperature remains below the NAT equilibrium temperature for several days [Fueglistaler *et al.*, 2002]. Therefore, it is

interesting to determine if there are important differences between our simulations and data related to not having wave clouds or evaporating ice releasing NAT in the model.

MLS and CALIPSO observations in 2008 [Lambert *et al.*, 2012] suggest that denitrification is associated with low number densities ($<10^{-3} \text{ cm}^{-3}$) of NAT with large effective radius ($>5\text{--}7 \mu\text{m}$) in early Antarctic winter before the temperature drops below the ice frost point. Based on this conclusion, we look at the 2010 simulation in our model compared with the observations from 24 to 28 May, which is a period of strong uptake of HNO_3 .

Figure 9 and 10 shows the simulated PSC properties and gas phase HNO_3 and H_2O compared with CALIPSO and MLS observations at 52 hPa (~490 K potential temperature). The simulated properties show the backscattering ratio, depolarization ratio, and mass mixing ratio. The optical properties from the model are plotted without noise in order to more clearly show how they overlap with each other. The depolarization for STS, NAT, ice, and total is defined to be the perpendicular backscatter for each constituent divided by the total parallel backscatter from all the PSCs.

Comparing Figures 9a–9j, the locations of the simulated STS and NAT generally capture the location of the observed PSCs. The observed backscattering ratio (~4) has the highest value in East Antarctic (around 40°E, 82°S). The simulated STS backscattering ratio (9c) is ~2.5. The highest backscatter in the simulations is provided by ice particles (Figure 9e) near the pole. In the CALIPSO observations, the PSCs above the Transantarctic Mountains and Ross Ice Shelf, around 160°E to 160°W and 80°S, show a low backscattering ratio (~1.3) as well as a high depolarization ratio (~0.5), which is consistent with the simulations if we consider the uncertainties due to noise. The simulation suggests that NAT/STS mixtures provide the backscattering ratio and the depolarization in this area. The simulation has large NAT particles ($>10 \mu\text{m}$) with a number density about $2\text{e}^{-4} \text{ cm}^{-3}$ (not shown in Figure 9). The gas phase HNO_3 comparison in Figure 10 also shows consistent denitrification between the model and MLS. The CALIPSO composition algorithm (Figures 9k–9m) finds less ice cloud coverage than simulated. The simulated ice has a mixing ratio ~0.5 ppm and a backscattering ratio of 4. The ice is present with STS over a large fraction of the geographic area near 82°S. CALIPSO identifies a few ice and Mix2 clouds in East Antarctic. However, the simulated NAT does not have strong backscatter signals in this area. Instead, ice particles show strong depolarization and backscatter there. The model may overestimate the ice cloud coverage because the model assumes that clouds completely fill the model grid cells. The overestimation of ice in the model may cause an inaccurate prediction of the heterogeneous chemistry that occurs in/on different kinds of PSCs in the model. H_2O in the model (Figure 10) shows a slight dehydration near the South Pole, but MLS observe does not have observations south of 82°S.

To answer question (1), the model does simulate large NAT particles. During the 24–28 May time period, the simulations suggest that large NAT particles are present above the Transantarctic Mountains and Ross Ice Shelf which agrees with the CALIPSO observation of low backscatter and high depolarization. Also, our model is consistent with denitrification due to large NAT particles during this time period as shown in Figure 10 and as discussed in section 4.4 below.

Figures 11 and 12 presents a comparison of the simulation with CALIPSO and MLS observations from 18 to 22 July 2010 at 52 hPa. Figures 11k–11p show the simulated PSC locations agree with the CALIPSO classified PSCs. CALIPSO shows high backscattering ratio (Figure 11a) and depolarization (Figure 11f) downstream (east) of the Antarctic Peninsula from 60°W to 60°E and a moderate backscattering ratio from 60°E to 180°. In our base case simulation, the backscattering ratio is high from 60°W to 60°E because of ice particles (Figure 11e). The STS (Figure 11c) increases the backscattering ratio moderately. From 60°E to 180°, the model shows a high backscatter (Figure 11b) and depolarization (Figure 11g) south of 80°S due to ice. In the area north of 80°S, the model shows a backscattering ratio ~1.2 and a depolarization ratio ~0.3 due to STS/NAT mixture. This backscattering ratio value is lower than the CALIPSO observation (~3) in this area, which suggests that a higher number density of small NAT particles is observed than is simulated. The modeled and observed HNO_3 in Figure 12 shows that the denitrification covers a large area south of 60°S and the modeled denitrification is slightly stronger than observed. The location and the amount of dehydration from the model agree with the MLS observation.

To explore how NAT forms during this period of time, we need to better isolate NAT clouds and ice clouds. We plot the PSC evolution from 14 to 20 July at 2 day intervals in Figure 13. To avoid the influence of falling particles from above, we draw the plots for 26 hPa. On 14–18 July (Figures 13a–13d and 13i–13l), the CALIPSO

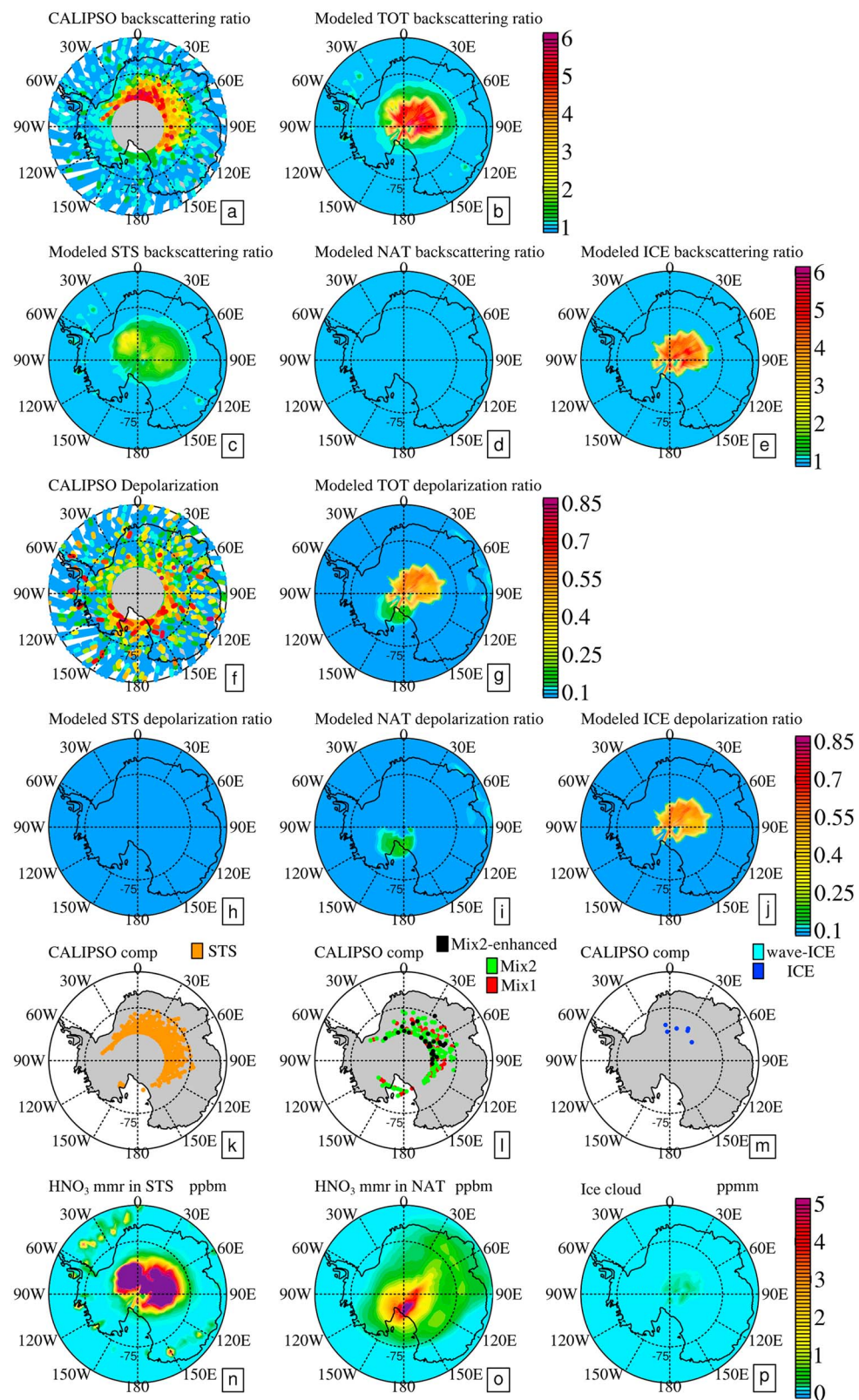


Figure 9. Simulated PSCs compared with CALIPSO observations at 52 hPa on 24–28 May 2010. (a–e) The maximum CALIPSO backscattering ratio compared with the modeled backscattering ratio. (f–j) The maximum CALIPSO depolarization ratio compared with the modeled depolarization ratio. (k–m) CALIPSO PSC compositions. (n–p) The modeled HNO₃ mass mixing ratio in STS and NAT, and H₂O mass mixing ratio in ice. The maximum latitude in the panels is 65°S.

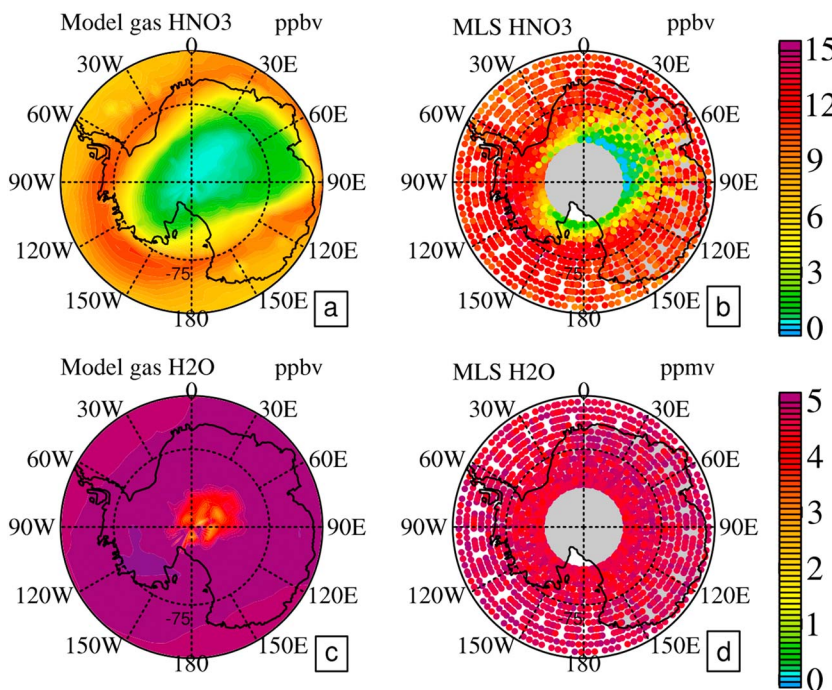


Figure 10. Simulated gas phase HNO₃ and H₂O compared with and MLS observation at 52 hPa on 24–28 May 2010. The maximum latitude in the panels is the same as in Figure 9.

algorithm suggests both STS (Figure 13a and 13c) and wave ice (Figures 13q and 13s) form at the Antarctic Peninsula. The model also shows a large amount of condensed HNO₃ (Figures 13e and 13g) and ice (Figures 13u and 13w) in these 2 days. The simulations suggest NAT particles (Figure 13o) form downwind of the Antarctic Peninsula (the wind blows from west to east). By 20 July (Figures 13m–13p), both STS (Figures 13d and 13h) and ice (Figures 13t and 13x) start to disappear, while NAT (Figures 13l and 13p) exists in a ring covering much of Antarctica. This sequence, shown in both observation and simulation, indicates that numerous NAT particles nucleated from STS or ice near the Antarctic Peninsula and were then transported downwind for several days until both the STS and ice evaporate or sediment. Figure 14 shows the optical properties from CALIPSO and the model on 20 July at 26 hPa. The CALIPSO observations show large backscattering ratio (Figure 14a) occurring from 60°S toward the South Pole and high depolarization ratio (Figure 14b). The large backscatter starts from ~60°S and east of Antarctic Peninsula (0° longitude) and circles into East Antarctic to ~60°E while it drifts toward the South Pole. However, the simulation overestimates the backscatter of ice (Figure 14c) and underestimates the backscatter from NAT/STS mixtures (Figure 14e) due to the large size and small number density of NAT. Therefore, a ring shape cannot be seen in the modeled backscattering ratio (Figure 14e). But the depolarization ratio (Figure 14f) in the model shows a moderate depolarization ratio for NAT in a ring shape. This shape is close to the shape seen in CALIPSO observation.

To answer question (2), the current model with homogeneous nucleation of NAT particles from STS is not able to simulate the numerous small NAT particles observed downwind of the Antarctic Peninsula (in July, for example, at 26 hPa). In future work, we will add temperature fluctuations due to the mountain wave to the model to test if homogeneous nucleation of NAT from STS with large temperature fluctuations leads to the formation of small NAT particles. We will also add the release of NAT from evaporating ice to determine if that process can form small NAT particles in a global model.

4.4. Sensitivity Tests for Denitrification and Dehydration

It is difficult to compare simulations of the PSC constituents in the global model with CALIPSO data. However, as we discussed in previous sections, our model is producing large NAT particles but not small ones, while both sizes are observed. Small NAT particles would not lead to denitrification directly due to their small size, but they might contribute to heterogeneous chemistry if their surface areas compete with those of STS. Large

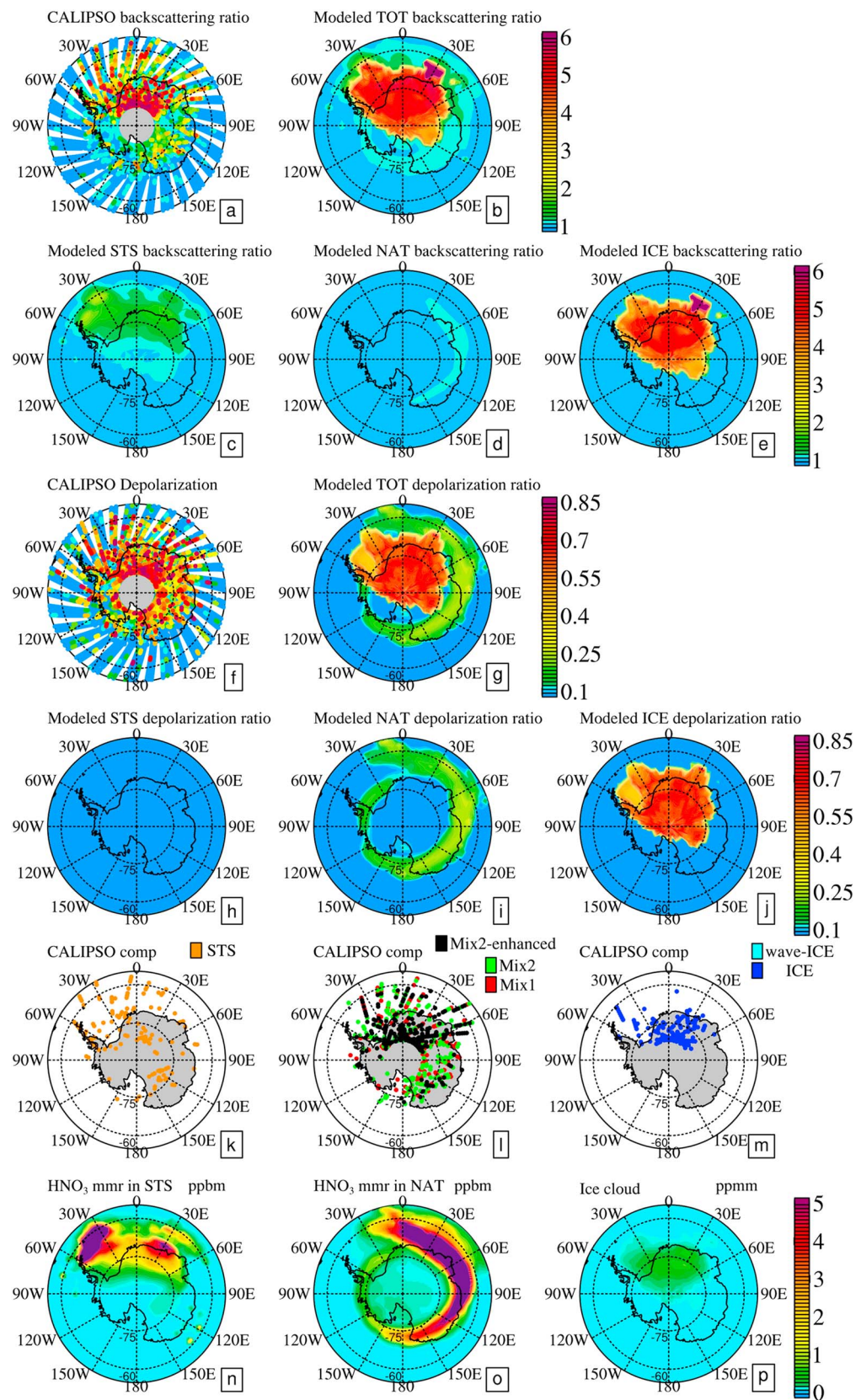


Figure 11. The modeled PSCs compared with CALIPSO at 52 hPa from 18 to 22 July 2010. The order of the plots is the same as Figure 9. The maximum latitude in the panels is 55°S.

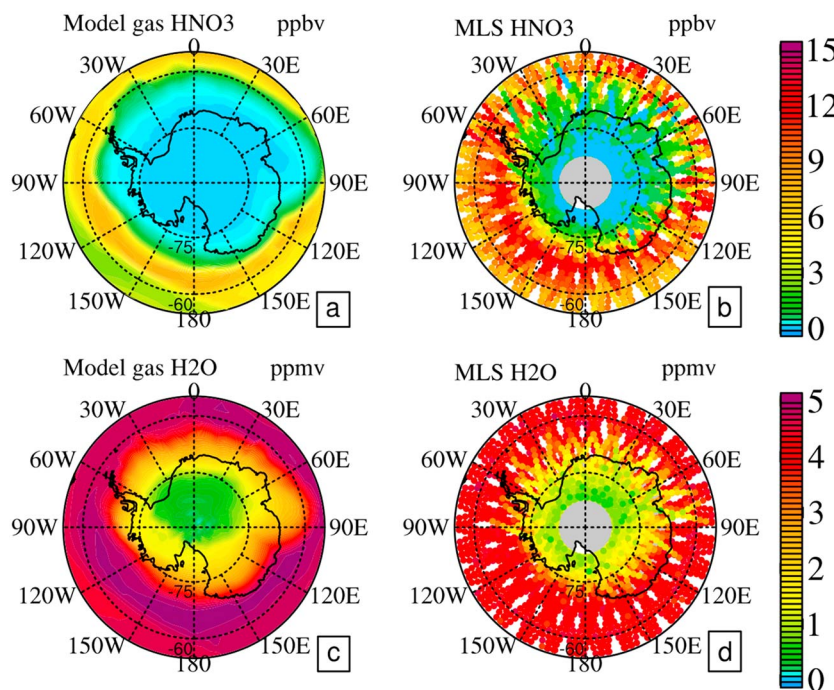


Figure 12. Simulated gas phase HNO₃ and H₂O compared with and MLS observation at 52 hPa on 18–22 July 2010. The maximum latitude in the panels is the same as in Figure 11.

NAT particles likely add little to heterogeneous chemistry due to their small surface areas but are important for denitrification. Here we explore how well the model is able to simulate the observed denitrification and dehydration.

Figures 15–19 show the simulated temperature, HNO₃, and H₂O evolution over the 2010 Antarctic winter at different pressure levels averaging the points between 80°S and 82°S. The figures also show MLS observations [*de Laat and van Weele, 2011*] from the same area. The line plots (Figures 15–17) show the observations (red), the base case (blue), a simulation with model temperatures reduced by 1.5 K (green), and a simulation with 100 times higher nucleation rate for NAT from STS with the original temperature (purple). The error bars for MLS observations in those line plots represent the systematic errors according to the validation of MLS version 3.3 [Schwartz *et al.*, 2008; Livesey *et al.*, 2011]; for temperature the estimated error is −2 K to +1 K, for HNO₃ the estimated error is 0.5 ppbv for 68 and 32 hPa and 1 ppbv for 21 hPa, and for H₂O the estimated error is 7% for all three levels.

Figure 15 shows that the temperature field from the simulation is within the MLS error bars but about 1.5 K warmer than the MLS observations as discussed by *Brakebusch et al.* [2013]. Figures 16 and 17 show that for the base case both the HNO₃ and H₂O fields are within the error bars of the observations at 68 hPa and generally within the error bar at 32 hPa until the end of August. However, the initial HNO₃ in Figure 16 is lower than observed at low pressures. At 21 hPa, the observation is higher than the simulation for both HNO₃ and H₂O during August. The simulated denitrification in Figure 16 and dehydration in Figure 17 are stronger than observed at 32 hPa in September and at 21 hPa in August, though the simulations and the data agree near the end of October. The HNO₃ evolution in Figure 16 shows that HNO₃ starts to increase after mid-July for 21 hPa, and after early September for 32 hPa and 68 hPa. The comparison between total HNO₃ (blue solid line) and gas phase HNO₃ (blue dashed line) for the base case shows that the increase of HNO₃ in later seasons is not because of the evaporation of condensed phase HNO₃. We find that the increase is due to the descent of the HNO₃ from upper layers as shown in Figure 18 for HNO₃ and Figure 19 for H₂O.

The −1.5 K sensitivity test in Figure 16 suggests that small temperature differences do not matter greatly to denitrification in the Antarctic, though *Zhu et al.* [2015] showed they did matter in the Arctic. As discussed in section 4.1, one could increase the simulated NAT and ice backscatter if the particles were more numerous and therefore smaller. Figures 16 and 18 show the impact of increasing the NAT nucleation rate by 100

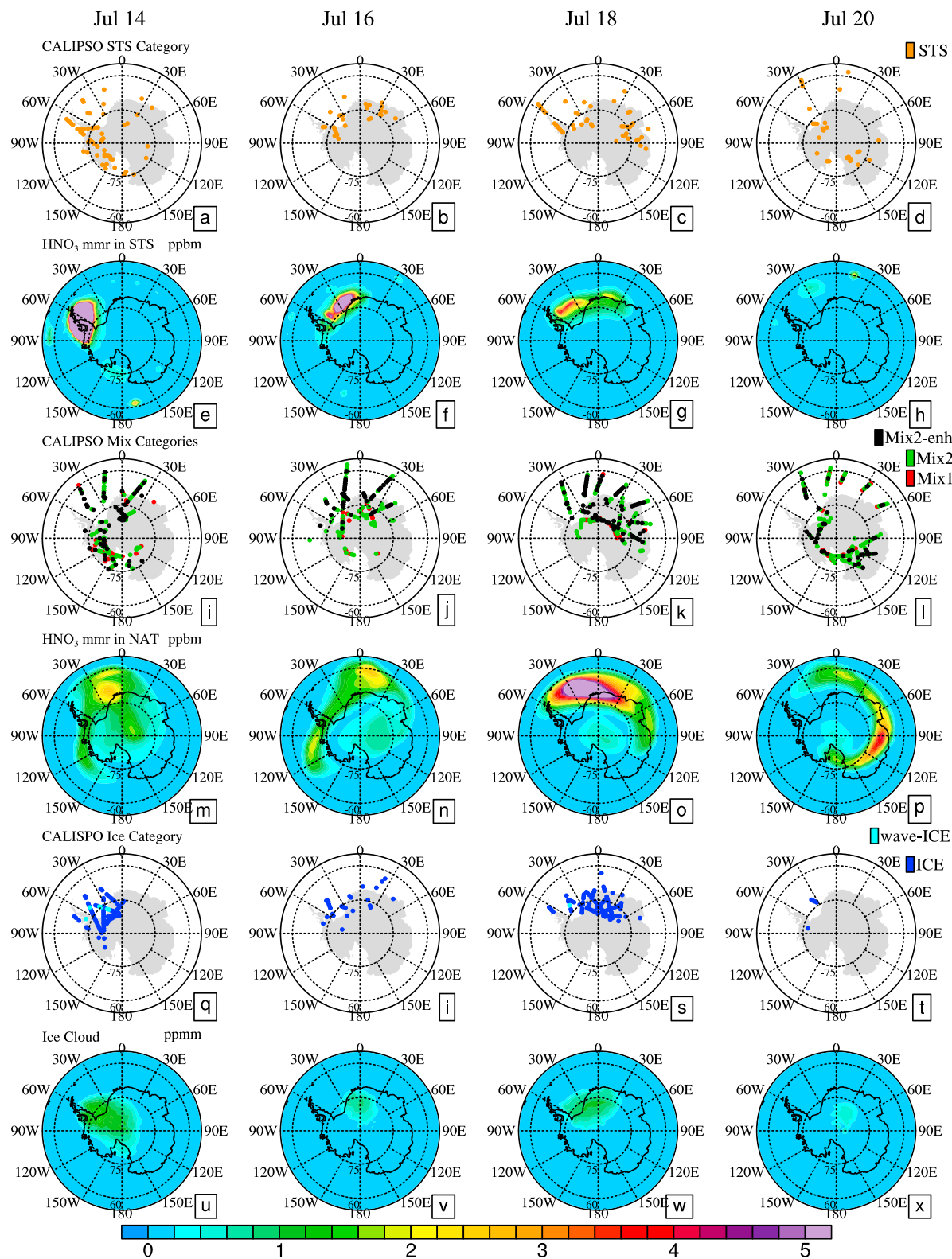


Figure 13. The simulated PSCs compared with CALIPSO and MLS data at 26 hPa from 14–20 July 2010 showing the evaluation of PSCs in this time period. (a–d) The CALIPSO STS category, (e–h) simulated condensed HNO₃ mass mixing ratio in STS, (i–l) the CALIPSO Mix categories, (m–p) the simulated condensed HNO₃ mass mixing ratio in NAT, (q–t) the CALIPSO ice category, and (u–x) the simulated ice mass mixing ratio. Figures 13a, 13e, 13i, 13m, 13q, and 13u are for 14 July, Figures 13b, 13f, 13j, 13n, 13i, and 13v are for 16 July, Figures 13c, 13g, 13k, 13o, 13s, and 13w are for 18 July, and Figures 13d, 13h, 13i, 13p, 13t, and 13x are for 20 July. The color bar represents the mass mixing ratio for the model results.

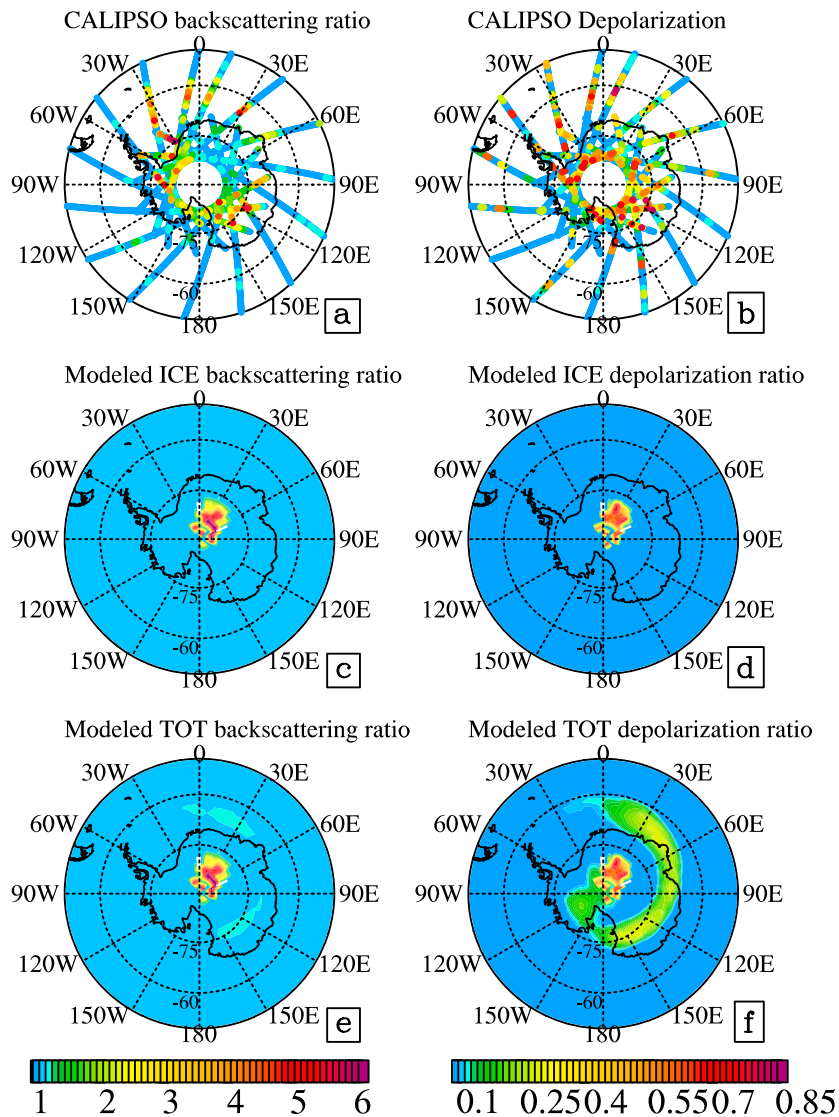


Figure 14. The backscattering ratio and depolarization ratio from the model and the CALIPSO at 26 hPa (22 km) on 20 July 2010. (a, b) CALIPSO data, (c, d) modeled ice only, and (e, f) the modeled total (ice + STS + NAT). The difference between Figures 14c and 14d and Figures 14e and 14f is mainly from the contribution from NAT/STS mixtures. The left color bar represents the backscattering ratio, and the right color bar represents the depolarization ratio.

(slopeflat100 case). The slopeflat100 case shows the denitrification occurs about 2 weeks or a month earlier than in the slopeflat case or than in observations. But the denitrification at the end of the season does not vary much between the slopeflat and slopeflat100 cases except at 21 hPa. At this pressure level, the slopeflat100 case shows a stronger denitrification than the other two model cases or observations. We conclude that increasing the homogeneous nucleation rate to achieve smaller NAT particles, which are required to better agree with CALIPSO data in some cases, produces worse agreement with denitrification. Therefore, the amount of large NAT particles calculated from our homogenous nucleation scheme in the base case [Zhu et al., 2015] is likely close to what happens in nature regarding to the amount of denitrification.

5. Conclusions and Discussions

We investigate the features of PSCs and related trace gases during the Antarctic winter of 2010, comparing simulations of the spatial and temporal distribution of PSCs and related gases with CALIPSO and MLS data. We listed four questions at the beginning of the paper.

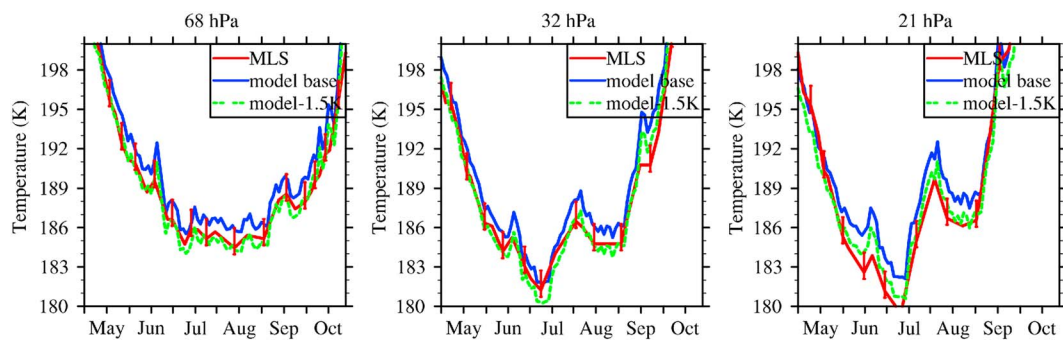


Figure 15. The temperature evolution over the 2010 Antarctic winter at three different pressure levels averaged over the points south of 80°S compared with MLS observations [de Laat and van Weele, 2011]. The red lines are the MLS temperature, the blue lines are the model temperature nudged with GOES-5, and the green lines show the model temperature minus 1.5 K.

The answer to question 1 is as follows: Several limitations of the CALIPSO PSC composition algorithm have been identified in the past (discussed in section 2.1). We additionally find that the CALIPSO algorithm tends to misclassify ice particles into Mix2 and Mix2-enhanced categories under dehydrated conditions, where they can be confused with NAT-containing mixtures.

The optical properties for ice are based on the mass-mixing ratio from the model output. We assume the ice number density is either 1% or 10% of STS number density. When we assume ice number density equivalent to 1% STS number, most of the ice particles are classified into Mix2-enhanced category. Pitts et al. [2013] previously showed under denitrified conditions with 5 ppbv gas phase HNO_3 that ice could be put into Mix2 category (shown in Figure 3). In this paper, we also show that ice can be misclassified due to both denitrification and dehydration. Figure 3 shows that mixed ice/STS clouds in a dehydrated atmosphere with 2.75 ppmv water vapor have a lower backscattering ratio and a higher depolarization ratio compared with the unperturbed situations. When the dehydration and denitrification occur at the same time, the points shift to even lower backscattering ratio. These lower ratios occur because the denitrification and dehydration strongly prohibits the growth of STS particles. Therefore, STS contributes less to the backscattering ratio and less to the parallel backscatter when the depolarization ratio is calculated in dehydrated conditions. When we assume an ice number density equivalent to 10% of STS number (Figure 4), more ice particles are identified in ice category ($1/R_{532} < 0.2$). In reality ice particles have a wide range of number densities and our model needs a better scheme to track them.

It has long been known that large NAT particles can have low backscatter mainly because they can have small surface areas despite having large mass. We show that such circumstances are common in our model. An example at 52 hPa in July suggests that the CALIPSO algorithm miss 31% of these clouds or fails to notice 15% of them inside STS clouds when the mass mixing ratio of NAT is larger than 4 ppbv.

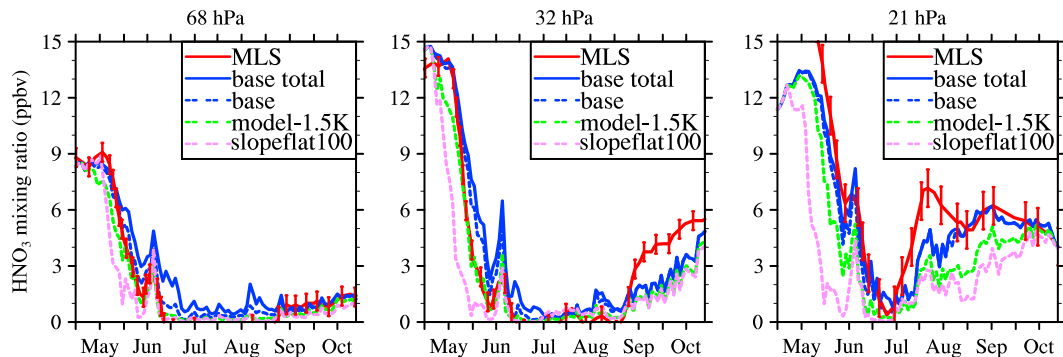


Figure 16. The HNO_3 evolution during the 2010 Antarctic winter at three different pressure levels averaging the points south of 80°S compared with MLS observations. The error bars in the top panels represents the systematic error as 0.5 ppbv for 68 and 32 hPa and 1 ppbv for 21 hPa [Livesey et al., 2011]. The colors represent MLS data in red, slopeflat case in blue (total HNO_3 in solid line and gas HNO_3 in dashed line), temperature -1.5 K case in green, and slopeflat100 case in purple.

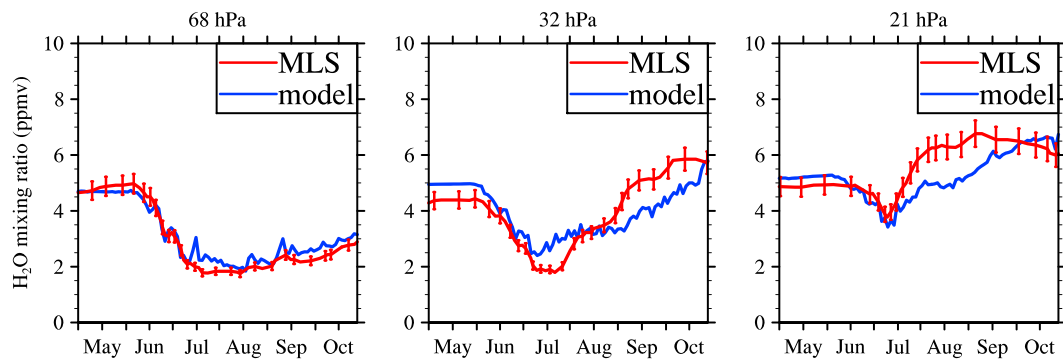


Figure 17. The simulated H_2O evolution over the 2010 Antarctic winter at three different pressure levels (top panels) averaged over the points south of 80°S compared with MLS observations. The error bar represents the systematic error of 7%. The colors represent MLS data in red, and the modeled case in blue. The H_2O fields are not changed relative to the base case for the slopeflat100 case and the -1.5K case simulated in Figure 16.

The answer to question 2 is as follows: We find that the total cloud coverage of PSCs from the model compares well with CALIPSO. However, in the simulations, many of the clouds classified in Mix categories contain ice so the model suggests ice clouds are more common than the CALIPSO classification suggests.

We compute the optical properties of PSCs from the model and classify them using the CALIPSO classification algorithm by Pitts *et al.* [2009]. We show the total area comparison as well as a comparison of PSCs in five

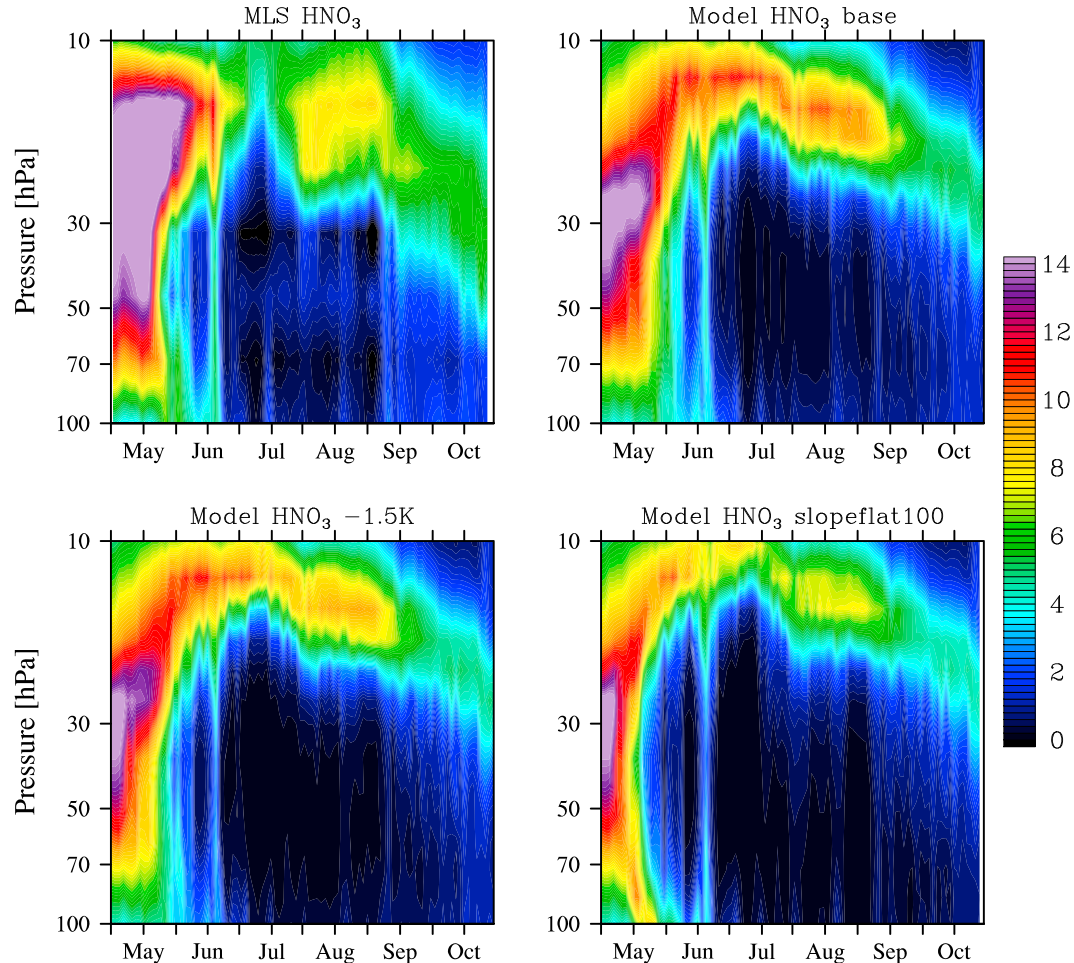


Figure 18. Contour plots showing the HNO_3 volume mixing ratio in ppbv averaged from 80°S to 82°S for MLS data and three simulations as in Figure 16.

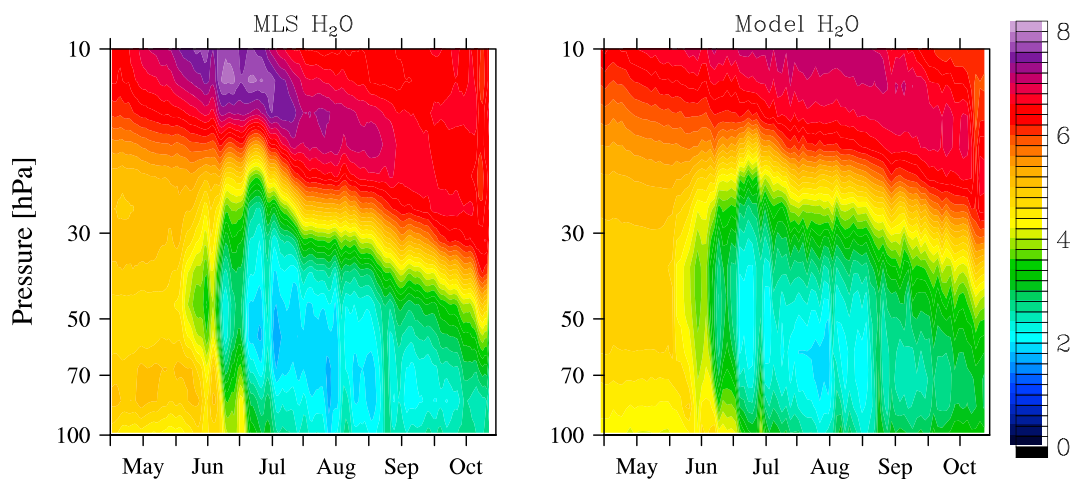


Figure 19. Contour plots showing the H_2O volume mixing ratio in ppmv averaged from 80°S to 82°S for MLS data and the simulation.

categories: STS, Mix1, Mix2, Mix2 enhanced, and ice. The PSC cloud coverage (Figure 6) from both the model and CALIPSO show that the PSCs for the 2010 Antarctic winter last from late May to September. The simulated and observed total areas agree within a few percent on average with a correlation coefficient of 0.831. The simulation and CALIPSO data both indicate that the STS dominates from late-May to mid-June as well as in September. Mixed clouds dominate CALIPSO observations in July and August, especially around 15 km in late May and 22 km in July and in late August. The Mix categories dominate in June and July in the simulation. Using the CALIPSO composition algorithm, both observations and simulations find ice clouds form in June, July, and August but usually contribute to a small fraction of PSCs.

Figure 8 shows that CALIPSO finds a bimodal distribution of the number of PSCs found at a given temperature for Mix2 and Mix2-enhanced categories. One of the modes is near the ice frost point and the other one is near the NAT equilibrium temperature. This distribution is a hint that the PSCs near the ice frost point are actually ice clouds or it could be new NAT particles nucleated from STS or ice near the frost point.

The answer to question 3 is as follows: Analysis of observations from CALIPSO and MLS clearly show that some PSCs are composed of NAT particles significantly larger than $1 \mu\text{m}$, while others have particles near $1 \mu\text{m}$ in size [e.g., *Lambert et al.*, 2012]. We analyze the PSC at 52 hPa from 24 to 28 May 2010 (Figure 9). The observations show a low backscattering ratio and a high depolarization ratio in the Transantarctic Mountain and Ross Ice sheet areas ($\sim 78\text{--}86^{\circ}\text{S}$, $160\text{--}200^{\circ}\text{E}$). This observation indicates large NAT particles form in the early season as discussed by previous research [*Lambert et al.*, 2012]. The modeled NAT appears in the observed location with low number density ($\sim 2\text{e}^{-4} \text{ cm}^{-3}$) and effective radius near or above $10 \mu\text{m}$.

In contrast to the large particle observations, the polar view of PSCs during the time from 14 to 22 July at 26 hPa demonstrates a small particle containing NAT belt downwind of the Palmer Peninsula (Figure 13). On 20 July, the CALIPSO observation shows high backscattering ratio and corresponding high depolarization ratio within 60°S , which suggest a high number density of small NAT particles. However, the simulations show a similar shape in the depolarization ratio plot but with low backscattering ratio. The observed formation of STS and wave ice particles (Figure 13) indicates that the Antarctic Peninsula probably triggers enhanced NAT formation.

We cannot simply increase the homogeneous nucleation rate to produce small NAT particles, because higher nucleation rates make denitrification occur too early in the simulations (Figure 16). The results suggest our homogeneous nucleation equations are functioning well to produce large, denitrifying NAT. However, another nucleation mechanism must make the small NAT particles. In the future, it will be necessary to include NAT forming from ice in the model microphysical processes. It may also be necessary to parameterize temperature fluctuations over the Antarctic Peninsula due to mountain waves.

The answer to questions 4 and 5 is as follows: The homogeneous NAT nucleation scheme applied in the Arctic for the winter of 2011 [*Zhu et al.*, 2015] (slopeflat case) correctly simulates the denitrification in the Antarctic

winter of 2010. We conclude that our nucleation scheme predicts the number and size of the NAT particles that are responsible for denitrification. The dehydration predicted by WACCM cloud model is also generally within the error bars of MLS observations.

We find that the modeled H₂O and HNO₃ are within the error bars of MLS observations at 68 hPa and mostly within the error bar before the end of August at 32 hPa. We also find that the simulated denitrification is not sensitive to changes in the temperature within the MLS error bars, though it was sensitive for a simulation conducted in the Arctic [Zhu *et al.*, 2015]. Increasing the NAT nucleation rate by 100 (slopeflat100 case) leads to an earlier denitrification about half a month or a month compared with observations. But at the end of the season, the HNO₃ amounts are very close for the model cases, except the 26 hPa, where the slopeflat100 case shows a lower HNO₃ amount than observed.

Several suggestions are made to improve the current model and the CALIPSO detection and classification schemes. For the modeling part, most important is to better simulate ice clouds and the NAT particles generated from ice. Further simulations of years other than 2010 in the Antarctic, or the Arctic, would also help to identify situations in which greater discrimination between the contributions of ice and NAT to the Mix categories might be possible. All the analyses indicate that we need a cloud model that predicts ice particle number, ice particle size, and cloud fraction so that we can better derive the ice cloud optical properties. We also need a microphysical model for ice PSCs that allows ice crystals to interact with nitric acid. Hoyle *et al.* [2013] and Groß *et al.* [2014] also suggest another way to form NAT from STS heterogeneously, because stratospheric sulfates commonly contain micrometeorites. When we compare the model results with CALIPSO, model resolution is also a problem when different PSC constituents are mixed within the grid box. The CALIPSO PSC detection and classification algorithm needs to consider dehydration and denitrification at the same time because the variation in the amount of material present, as well as instrument noise, produces a considerable spread in the values of the backscatter and depolarization, which mixes particle compositions across the possible choices defined by CALIPSO classification algorithm.

Appendix A: NAT and Ice Depolarization From T-Matrix Code

In order to obtain the NAT and ice depolarization, we apply the T-matrix code with the following assumption: We use real refractive indices of 1.50 for NAT with an aspect ratio of 0.9 and a real index of 1.308 for ice with an aspect ratio of 0.95. Those assumptions are different from the assumptions by Pitts *et al.* [2009], which assume an aspect ratio of 1.2 for both ice and NAT particles. However, the values we use are consistent with the current CALIPSO team choices for aspect ratio. Figures A1 and A2 show how the aspect ratio influences the depolarization of NAT and ice particles as a function of particle effective radius. In both figures, the depolarization is relatively low for an aspect ratio of 1.2 when the radius is over 2 μm . However, when we assume the aspect ratio of 0.9 for NAT or 0.95 for ice, the depolarization ratio is large over a wide radius range from 2 or 3 to as large as 10 μm .

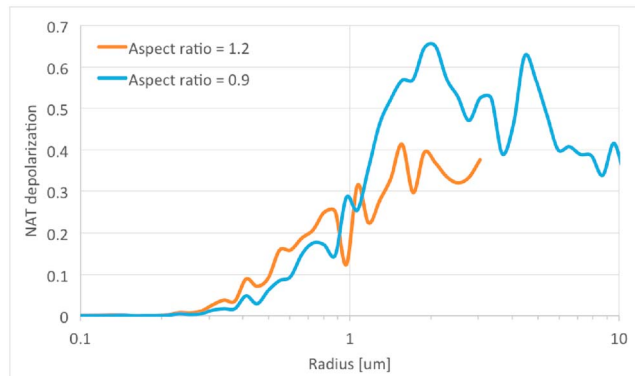


Figure A1. The NAT depolarization as a function of particle effective radius with particle aspect ratio of 1.2 (orange line) and aspect ratio of 0.9 (blue line).

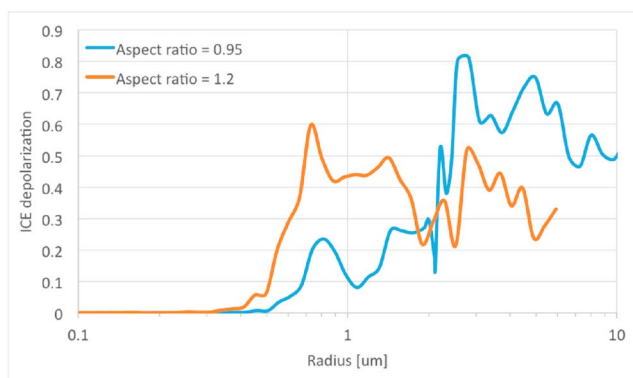


Figure A2. The ice depolarization as a function of particle effective radius with particle aspect ratio of 1.2 (orange line) and aspect ratio of 0.95 (blue line).

Acknowledgments

The work at the University of Colorado was supported by NASA grant NNX09AK71G from the AURA satellite project. The work at the Jet Propulsion Laboratory, California Institute of Technology, was carried out under a contract with the National Aeronautics and Space Administration. We thank Lamont Poole at NASA Langley Research Center for his help with the CALIPSO classification algorithm. We thank A.T.J. de Laat from Royal Netherlands Meteorological Institute for his help with MLS data. We thank Jens-Uwe Groß and Ines Tritscher from Forschungszentrum Jülich for their help with the noise uncertainty estimation for the CALIPSO algorithm. We would like to acknowledge high-performance computing support from Yellowstone (ark:/85065/d7wd3xhc) provided by NCAR's Computational and Information Systems Laboratory, sponsored by the National Science Foundation. The source code for WACCM/CARMA model used in this study is freely available at <http://www2.cesm.ucar.edu/> upon registration. The developing version of this model, the data, and input files necessary to reproduce the experiments are available from the authors upon request (yunqian.zhu@colorado.edu). The data are archived at the Toon Aerosol Research Group computers.

References

- Bardeen, C. G., A. Gettelman, E. J. Jensen, A. Heymsfield, A. J. Conley, J. Delanoë, M. Deng, and O. B. Toon (2013), Improved cirrus simulations in a general circulation model using CARMA sectional microphysics, *J. Geophys. Res. Atmos.*, **118**, 11,679–11,697, doi:10.1002/2013JD020193.
- Brakebusch, M., C. E. Randall, D. E. Kinnison, S. Tilmes, M. L. Santee, and G. L. Manney (2013), Evaluation of whole atmosphere community climate model simulations of ozone during Arctic winter 2004–2005, *J. Geophys. Res. Atmos.*, **118**, 2673–2688, doi:10.1002/jgrd.50226.
- Browell, E. V., C. F. Butler, S. Ismail, P. A. Robinette, A. F. Carter, N. S. Higdon, O. B. Toon, M. R. Schoeberl, and A. F. Tuck (1990), Airborne lidar observations in the wintertime Arctic stratosphere: Polar stratospheric clouds, *Geophys. Res. Lett.*, **17**, 385–388, doi:10.1029/GL017i004p00385.
- Carlsaw, K. S., B. Luo, and T. Peter (1995), An analytic expression for the composition of aqueous $\text{HNO}_3\text{-H}_2\text{SO}_4$ stratospheric aerosols including gas phase removal of HNO_3 , *Geophys. Res. Lett.*, **22**, 1877–1880, doi:10.1029/95GL01668.
- Carlsaw, K. S., M. Wirth, A. Tsias, B. P. Luo, A. Dörnbrack, M. Leutbecher, H. Volkert, W. Renger, J. T. Bacmeister, and T. Peter (1998), Particle microphysics and chemistry in remotely observed mountain polar stratospheric clouds, *J. Geophys. Res.*, **103**, 5785–5796, doi:10.1029/97JD03626.
- Carlsaw, K. S., J. A. Kettleborough, M. J. Northway, S. Davies, R.-S. Gao, D. W. Fahey, D. G. Baumgardner, M. P. Chipperfield, and A. Kleinböhl (2002), A vortex-scale simulation of the growth and sedimentation of large nitric acid hydrate particles, *J. Geophys. Res.*, **107(D20)**, 8300, doi:10.1029/2001JD000467.
- Chipperfield, M. P., and J. A. Pyle (1998), Model sensitivity studies of Arctic ozone depletion, *J. Geophys. Res.*, **103**, 28,389–28,403, doi:10.1029/98JD01960.
- de Laat, A. T. J., and M. van Weele (2011), The 2010 Antarctic ozone hole: Observed reduction in ozone destruction by minor sudden stratospheric warmings, *Sci. Rep.*, **1**, 38.
- Dhaniyala, S., K. A. McKinney, and P. O. Wennberg (2002), Lee-wave clouds and denitrification of the polar stratosphere, *Geophys. Res. Lett.*, **29(9)**, 1322, doi:10.1029/2001GL013900.
- Dye, J. E., D. Baumgardner, B. W. Gandrud, S. R. Kawa, K. K. Kelly, M. Loewenstein, G. V. Ferry, K. R. Chan, and B. L. Gary (1992), Particle size distributions in Arctic polar stratospheric clouds, growth and freezing of sulfuric acid droplets, and implications for cloud formation, *J. Geophys. Res.*, **97**, 8015–8034, doi:10.1029/91JD02740.
- Eckermann, S. D., L. Hoffmann, D. Höpfner, D. L. Wu, and M. J. Alexander (2009), Antarctic NAT PSC belt of June 2003: Observational validation of the mountain wave seeding hypothesis, *Geophys. Res. Lett.*, **36**, L02807, doi:10.1029/2008GL036629.
- Engel, I., B. P. Luo, M. C. Pitts, L. R. Poole, C. R. Hoyle, J.-U. Groß, A. Dörnbrack, and T. Peter (2013), Heterogeneous formation of polar stratospheric clouds—Part 2: Nucleation of ice on synoptic scales, *Atmos. Chem. Phys.*, **13**(21), 10,769–10,785, doi:10.5194/acp-13-10769-2013.
- English, J. M., O. B. Toon, M. J. Mills, and F. Yu (2011), Microphysical simulations of new particle formation in the upper troposphere and lower stratosphere, *Atmos. Chem. Phys.*, **11**(17), 9303–9322, doi:10.5194/acp-11-9303-2011.
- Fahey, D. W., et al. (2001), The detection of large HNO_3 -containing particles in the winter Arctic stratosphere, *Science*, **291**(5506), 1026–1031, doi:10.1126/science.1057265.
- Farman, J. C., B. G. Gardiner, and J. D. Shanklin (1985), Large losses of total ozone in Antarctica reveal seasonal ClO_x/NO_x interaction, *Nature*, **315**(6016), 207–210.
- Fueglistaler, S., B. P. Luo, C. Voigt, K. S. Carlsaw, and T. Peter (2002), NAT-rock formation by mother clouds: A microphysical model study, *Atmos. Chem. Phys.*, **2**(2), 93–98, doi:10.5194/acp-2-93-2002.
- Garcia, R. R., D. R. Marsh, D. E. Kinnison, B. A. Boville, and F. Sassi (2007), Simulation of secular trends in the middle atmosphere, 1950–2003, *J. Geophys. Res.*, **112**, D09301, doi:10.1029/2006JD007485.
- Groß, J.-U., et al. (2014), Nitric acid trihydrate nucleation and denitrification in the Arctic stratosphere, *Atmos. Chem. Phys.*, **14**(2), 1055–1073, doi:10.5194/acp-14-1055-2014.
- Hanson, D., and K. Mauersberger (1988), Laboratory studies of the nitric acid trihydrate: Implications for the south polar stratosphere, *Geophys. Res. Lett.*, **15**, 855–858, doi:10.1029/GL015i008p00855.
- Hanson, D. R., A. R. Ravishankara, and S. Solomon (1994), Heterogeneous reactions in sulfuric acid aerosols: A framework for model calculations, *J. Geophys. Res.*, **99**, 3615–3629, doi:10.1029/93JD02932.
- Höpfner, M., et al. (2006a), MIPAS detects Antarctic stratospheric belt of NAT PSCs caused by mountain waves, *Atmos. Chem. Phys.*, **6**(5), 1221–1230, doi:10.5194/acp-6-1221-2006.
- Höpfner, M., et al. (2006b), Spectroscopic evidence for NAT, STS, and ice in MIPAS infrared limb emission measurements of polar stratospheric clouds, *Atmos. Chem. Phys.*, **6**(5), 1201–1219, doi:10.5194/acp-6-1201-2006.

- Hoyle, C. R., I. Engel, B. P. Luo, M. C. Pitts, L. R. Poole, J.-U. Grooß, and T. Peter (2013), Heterogeneous formation of polar stratospheric clouds—Part 1: Nucleation of nitric acid trihydrate (NAT), *Atmos. Chem. Phys.*, 13(18), 9577–9595, doi:10.5194/acp-13-9577-2013.
- Jensen, E. J., and O. B. Toon (1994), Ice nucleation in the upper troposphere: Sensitivity to aerosol number density, temperature, and cooling rate, *Geophys. Res. Lett.*, 21, 2019–2022, doi:10.1029/94GL01287.
- Kawa, S. R., et al. (1997), Activation of chlorine in sulfate aerosol as inferred from aircraft observations, *J. Geophys. Res.*, 102, 3921–3933, doi:10.1029/96JD01992.
- Kelly, K. K., A. F. Tuck, L. E. Heidt, M. Loewenstein, J. R. Podolske, S. E. Strahan, and J. F. Vedder (1990), A comparison of ER-2 measurements of stratospheric water vapor between the 1987 Antarctic and 1989 Arctic airborne missions, *Geophys. Res. Lett.*, 17, 465–468, doi:10.1029/GL017004p00465.
- Kelly, K. K., et al. (1989), Dehydration in the lower Antarctic stratosphere during late winter and early spring, 1987, *J. Geophys. Res.*, 94, 11,317–11,357, doi:10.1029/JD094iD09p11317.
- Kinnison, D. E., et al. (2007), Sensitivity of chemical tracers to meteorological parameters in the MOZART-3 chemical transport model, *J. Geophys. Res.*, 112, D20302, doi:10.1029/2006JD007879.
- Kühl, S., A. Dörnbrack, W. Wilms-Grabe, B.-M. Sinnhuber, U. Platt, and T. Wagner (2004), Observational evidence of rapid chlorine activation by mountain waves above northern Scandinavia, *J. Geophys. Res.*, 109, D22309, doi:10.1029/2004JD004797.
- Lambert, A., M. L. Santee, D. L. Wu, and J. H. Chae (2012), A-train CALIPR and MLS observations of early winter Antarctic polar stratospheric clouds and nitric acid in 2008, *Atmos. Chem. Phys.*, 12(6), 2899–2931.
- Livesey, N. J., W. G. Read, L. Froidevaux, A. Lambert, G. L. Manney, H. C. Pumphrey, M. L. Santee, M. J. Schwartz, S. Wang, and R. E. Cofield (2011), Version 3.3 level 2 data quality and description document, Jet Propulsion Laboratory D-33509.
- McCormick, M. P., H. M. Steele, P. Hamill, W. P. Chu, and T. J. Swissler (1982), Polar stratospheric cloud sightings by SAM II, *J. Atmos. Sci.*, 39(6), 1387–1397, doi:10.1175/1520-0469(1982)039<1387:PSCSBS>2.0.CO;2.
- Mishchenko, M. I., and L. D. Travis (1998), Capabilities and limitations of a current FORTRAN implementation of the T-matrix method for randomly oriented, rotationally symmetric scatterers, *J. Quant. Spectrosc. Radiat. Transfer*, 60(3), 309–324, doi:10.1016/S0022-4073(98)00008-9.
- Murphy, D. M., and T. Koop (2005), Review of the vapour pressures of ice and supercooled water for atmospheric applications, *Q. J. R. Meteorol. Soc.*, 131(608), 1539–1565.
- Nedoluha, G. E., R. M. Bevilacqua, K. W. Hoppel, M. Daehler, E. P. Shettle, J. H. Hornstein, M. D. Fromm, J. D. Lumpe, and J. E. Rosenfield (2000), POAM III measurements of dehydration in the Antarctic lower stratosphere, *Geophys. Res. Lett.*, 27, 1683–1686, doi:10.1029/1999GL011087.
- Pitts, M. C., and L. R. Poole (2014), A synopsis of CALIPSO polar stratospheric cloud observations from 2006–2014, SPIE, 9246, 92460B p.
- Pitts, M. C., L. R. Poole, and L. W. Thomason (2009), CALIPSO polar stratospheric cloud observations: Second-generation detection algorithm and composition discrimination, *Atmos. Chem. Phys.*, 9(19), 7577–7589, doi:10.5194/acp-9-7577-2009.
- Pitts, M. C., L. W. Thomason, L. R. Poole, and D. M. Winker (2007), Characterization of Polar Stratospheric Clouds with spaceborne lidar: CALIPSO and the 2006 Antarctic season, *Atmos. Chem. Phys.*, 7(19), 5207–5228, doi:10.5194/acp-7-5207-2007.
- Pitts, M. C., L. R. Poole, A. Dörnbrack, and L. W. Thomason (2011), The 2009–2010 Arctic polar stratospheric cloud season: A CALIPSO perspective, *Atmos. Chem. Phys.*, 11(5), 2161–2177, doi:10.5194/acp-11-2161-2011.
- Pitts, M. C., L. R. Poole, A. Lambert, and L. W. Thomason (2013), An assessment of CALIOP polar stratospheric cloud composition classification, *Atmos. Chem. Phys.*, 13(6), 2975–2988, doi:10.5194/acp-13-2975-2013.
- Reinecker, M. M., M. J. Suarez, R. Todling, J. Bacmeister, L. Takacs, H. C. Liu, W. Gu, M. Sienkiewicz, R. D. Koster, and R. Gelaro (2008), The GEOS-5 data assimilation system—documentation of versions 5.0. 1, 5.1. 0, NASA Tech Rep. TM-2007, 104606.
- Schoeberl, M. R. (2007), The EOS Aura mission, in *Observing Systems for Atmospheric Composition*, pp. 64–70, Springer, New York.
- Schwartz, M. J., et al. (2008), Validation of the Aura Microwave Limb Sounder temperature and geopotential height measurements, *J. Geophys. Res.*, 113, D15S11, doi:10.1029/2007JD008783.
- Solomon, S., R. R. Garcia, F. S. Rowland, and D. J. Wuebbles (1986), On the depletion of Antarctic ozone, *Nature*, 321(6072), 755–758.
- Solomon, S., J. Haskins, D. J. Ivy, and F. Min (2014), Fundamental differences between Arctic and Antarctic ozone depletion, *Proc. Natl. Acad. Sci. U.S.A.*, 111(17), 6220–6225, doi:10.1073/pnas.1319307111.
- Solomon, S., D. Kinnison, J. Bandoro, and R. Garcia (2015), Simulation of polar ozone depletion: An update, *J. Geophys. Res. Atmos.*, 120, 7958–7974, doi:10.1002/2015JD023365.
- Stanford, J. L., and J. S. Davis (1974), A century of stratospheric cloud reports: 1870–1972, *Bull. Am. Meteorol. Soc.*, 55(3), 213–219, doi:10.1175/1520-0477(1974)055<0213:ACOSCR>2.0.CO;2.
- Tabazadeh, A., Y. S. Djikaev, P. Hamill, and H. Reiss (2002), Laboratory evidence for surface nucleation of solid polar stratospheric cloud particles, *J. Phys. Chem. A*, 106(43), 10,238–10,246, doi:10.1021/jp021045k.
- Tizek, H., E. Knozinger, and H. Grothe (2004), Formation and phase distribution of nitric acid hydrates in the mole fraction range $x\text{HNO}_3 < 0.25$: A combined XRD and IR study, *Phys. Chem. Chem. Phys.*, 6(5), 972–979, doi:10.1039/B310672A.
- Toon, O. B., R. P. Turco, and P. Hamill (1990), Denitrification mechanisms in the polar stratospheres, *Geophys. Res. Lett.*, 17, 445–448, doi:10.1029/GL017004p00445.
- Toon, O. B., P. Hamill, R. P. Turco, and J. Pinto (1986), Condensation of HNO_3 and HCl in the winter polar stratospheres, *Geophys. Res. Lett.*, 13, 1284–1287, doi:10.1029/GL013i012p01284.
- Toon, O. B., A. Tabazadeh, E. V. Browell, and J. Jordan (2000), Analysis of lidar observations of Arctic polar stratospheric clouds during January 1989, *J. Geophys. Res.*, 105, 20,589–20,615, doi:10.1029/2000JD900144.
- Toon, O. B., R. P. Turco, D. Westphal, R. Malone, and M. Liu (1988), A multidimensional model for aerosols: Description of computational analogs, *J. Atmos. Sci.*, 45(15), 2123–2144, doi:10.1175/1520-0469(1988)045<2123:AMMFAD>2.0.CO;2.
- Vömel, H., S. J. Oltmans, D. J. Hofmann, T. Deshler, and J. M. Rosen (1995), The evolution of the dehydration in the Antarctic stratospheric vortex, *J. Geophys. Res.*, 100, 13,919–13,926, doi:10.1029/95JD01000.
- Waibel, A. E., T. Peter, K. S. Carslaw, H. Oelhaf, G. Wetzel, P. J. Crutzen, U. Pöschl, A. Tsias, E. Reimer, and H. Fischer (1999), Arctic ozone loss due to denitrification, *Science*, 283(5410), 2064–2069, doi:10.1126/science.283.5410.2064.
- Wang, Z., G. Stephens, T. Deshler, C. Trepte, T. Parish, D. Vane, D. Winker, D. Liu, and L. Adhikari (2008), Association of Antarctic polar stratospheric cloud formation on tropospheric cloud systems, *Geophys. Res. Lett.*, 35, L13806, doi:10.1029/2008GL034209.
- Wegner, T., D. E. Kinnison, R. R. Garcia, and S. Solomon (2013), Simulation of polar stratospheric clouds in the specified dynamics version of the whole atmosphere community climate model, *J. Geophys. Res. Atmos.*, 118, 4991–5002, doi:10.1002/jgrd.50415.
- Wegner, T., J.-U. Grooß, M. von Hobe, F. Stroh, O. Sumińska-Ebersoldt, C. M. Volk, E. Hösen, V. Mitev, G. Shur, and R. Müller (2012), Heterogeneous chlorine activation on stratospheric aerosols and clouds in the Arctic polar vortex, *Atmos. Chem. Phys.*, 12(22), 11,095–11,106, doi:10.5194/acp-12-11095-2012.

- Winker, D. M., W. H. Hunt, and M. J. McGill (2007), Initial performance assessment of CALIOP, *Geophys. Res. Lett.*, 34, L19803, doi:10.1029/2007GL030135.
- Winker, D. M., M. A. Vaughan, A. Omar, Y. Hu, K. A. Powell, Z. Liu, W. H. Hunt, and S. A. Young (2009), Overview of the CALIPSO mission and CALIOP data processing algorithms, *J. Atmos. Oceanic Technol.*, 26(11), 2310–2323, doi:10.1175/2009JTECHA1281.1.
- Zasetsky, A. Y., K. Gilbert, I. Galkina, S. McLeod, and J. J. Sloan (2007), Properties of polar stratospheric clouds obtained by combined ACE-FTS and ACE-Imager extinction measurements, *Atmos. Chem. Phys. Discuss.*, 7(5), 13,271–13,290, doi:10.5194/acpd-7-13271-2007.
- Zhu, Y., O. B. Toon, A. Lambert, D. E. Kinnison, M. Brakebusch, C. G. Bardeen, M. J. Mills, and J. M. English (2015), Development of a polar stratospheric cloud model within the Community Earth System Model using constraints on type I PSCs from the 2010–2011 Arctic winter, *J. Adv. Model. Earth Syst.*, 7, 551–585, doi:10.1002/2015MS000427.